Nucleosynthetic yields of $Z = 10^{-5}$ intermediate-mass stars[⋆]

P. Gil-Pons[1,2], C. L. Doherty[3,4], J. Gutiérrez[1,2], S. W. Campbell[4], L. Siess[5], and J. C. Lattanzio[4]

[1] EETAC, Universitat Politècnica de Catalunya, Campus Baix Llobregat, C3, 08840 Castelldefels, Spain
  e-mail: pilar.gil@upc.edu
[2] Institut d'Estudis Espacials de Catalunya, Ed-Nexus Campus Nord, Barcelona, Spain
[3] Konkoly Observatory, Hungarian Academy of Sciences, 1121 Budapest, Hungary
[4] School of Physics and Astronomy, Monash University, Clayton, Australia
[5] Institut d'Astronomie et d'Astrophysique, Université Libre de Bruxelles, ULB, Belgium

Received 5 December 2019 / Accepted 15 October 2020

ABSTRACT

Context. Observed abundances of extremely metal-poor stars in the Galactic halo hold clues for understanding the ancient universe. Interpreting these clues requires theoretical stellar models in a wide range of masses in the low-metallicity regime. The existing literature is relatively rich with extremely metal-poor massive and low-mass stellar models. However, relatively little information is available on the evolution of intermediate-mass stars of $Z \lesssim 10^{-5}$, and the impact of the uncertain input physics on the evolution and nucleosynthesis has not yet been systematically analysed.
Aims. We aim to provide the nucleosynthetic yields of intermediate-mass $Z = 10^{-5}$ stars between 3 and 7.5 $M_\odot$, and quantify the effects of the uncertain wind rates. We expect these yields could eventually be used to assess the contribution to the chemical inventory of the early universe, and to help interpret abundances of selected C-enhanced extremely metal-poor (CEMP) stars.
Methods. We compute and analyse the evolution of surface abundances and nucleosynthetic yields of $Z = 10^{-5}$ intermediate-mass stars from their main sequence up to the late stages of their thermally pulsing (Super) AGB phase, with different prescriptions for stellar winds. We use the postprocessing code MONSOON to compute the nucleosynthesis based on the evolution structure obtained with the Monash-Mount Stromlo stellar evolution code MONSTAR. By comparing our models and others from the literature, we explore evolutionary and nucleosynthetic trends with wind prescriptions and with initial metallicity (in the very low-Z regime). We also compare our nucleosynthetic yields to observations of CEMP-s stars belonging to the Galactic halo.
Results. The yields of intermediate-mass extremely metal-poor stars reflect the effects of very deep or corrosive second dredge-up (for the most massive models), superimposed with the combined signatures of hot-bottom burning and third dredge-up. Specifically, we confirm the reported trend that models with initial metallicity $Z_{ini} \lesssim 10^{-3}$ give positive yields of ^{12}C, ^{15}N, ^{16}O, and ^{26}Mg. The ^{20}Ne, ^{21}Ne, and ^{24}Mg yields, which were reported to be negative at $Z_{ini} \gtrsim 10^{-4}$, become positive for $Z = 10^{-5}$. The results using two different prescriptions for mass-loss rates differ widely in terms of the duration of the thermally pulsing (Super) AGB phase, overall efficiency of the third dredge-up episode, and nucleosynthetic yields. We find that the most efficient of the standard wind rates frequently used in the literature seems to favour agreement between our yield results and observational data. Regardless of the wind prescription, all our models become N-enhanced EMP stars.

Key words. stars: abundances – stars: AGB and post-AGB – stars: evolution – stars: Population II

1. Introduction

Stellar evolution models and nucleosynthetic yields of extremely metal-poor stars (EMPs) are important pieces of the big puzzle of the chemical evolution history of the universe. EMPs are those with $Z \lesssim 10^{-5}$ or [Fe/H] $\lesssim -3$ (Beers & Christlieb 2005)[1]. A number of interesting works have been presented in this field over the last few decades (e.g. Fujimoto et al. 1984, 2000; Cassisi & Castellani 1993; Marigo et al. 2001; Chieffi et al. 2001; Siess et al. 2002; Denissenkov & Herwig 2003; Herwig et al. 2014; Gil-Pons et al. 2008; Lau et al. 2009; Campbell & Lattanzio 2008; Suda & Fujimoto 2010; Gil-Pons et al. 2013, to mention

a few). However, the evolution, nucleosynthesis, and even the fates of intermediate-mass stars between ∼3 and ∼7–9 $M_\odot$ is still poorly constrained, and theoretical results from different authors frequently show substantial differences (Gil-Pons et al. 2018).

The above mentioned works notwithstanding, the amount of results reported in this metallicity regime is much smaller than those dedicated to intermediate-mass stars of higher metallicity (see the review by Karakas & Lattanzio 2014, and references therein). The main reasons for this are likely linked to the historical difficulty in the detection of stars at the lowest metallicities; the very substantial uncertainties which hamper our knowledge of these stars (mainly related to the treatment of convection, mixing, and mass-loss rates, which cannot be properly calibrated by observations); the fact that evolutionary calculations of these objects tend to involve the computation of huge numbers of thermal pulses (Lau et al. 2008); and finally the limitations of one-dimensional hydrostatic codes for computing certain phases of the evolution of low-metallicity stars (Woodward et al. 2015), such as dual-shell flashes (Campbell & Lattanzio 2008; Mocák et al. 2010). These limitations in our knowledge of the evolution

---

[⋆] The yield tables are only available at the CDS via anonymous ftp to cdsarc.u-strasbg.fr (130.79.128.5) or via http://cdsarc.u-strasbg.fr/viz-bin/cat/J/A+A/645/A10

[1] Metallicity may be expressed as the logarithm of the iron-to-hydrogen number abundance ratio relative to the Sun, according to the standard expression [Fe/H] = $\log (N_{Fe}/N_H)_\star - \log (N_{Fe}/N_H)_\odot$. Abundance ratios of an element or isotope X over iron can also expressed relative to solar values as [X/Fe] = $\log (N_X/N_{Fe})_\star - \log (N_X/N_{Fe})_\odot$.

and fates of intermediate-mass EMPs (IM EMPs) necessarily imply an even poorer understanding of the associated nucleosynthesis, and therefore our knowledge of their yields is restricted to a limited number of isotopes (see, e.g. Abia et al. 2001; Iwamoto 2009; Gil-Pons et al. 2013).

The lack of nucleosynthetic yields of intermediate-mass stars at the lowest Z-regime ($Z \lesssim 10^{-5}$) is also reflected in the inputs of chemical-evolution models (see, e.g. Chiappini et al. 1997; Kobayashi et al. 2006; Tsujimoto & Bekki 2012; Brusadin et al. 2013; Mollá et al. 2015; Côté et al. 2016; Matteucci et al. 2016; Spitoni et al. 2017; Prantzos et al. 2018; Millán-Irigoyen et al. 2020 and references therein). Frequently used sets of yields, such as those used by van den Hoek & Groenewegen (1997), Marigo (2001), or Gavilán et al. (2005, 2006) are based on a synthetic approach for the treatment of the thermally pulsing asymptotic giant branch, TP-AGB. Ventura & D'Antona (2005, 2010), Siess (2010), Karakas (2010), Doherty et al. (2014a,b) and Ritter et al. (2018) presented detailed evolution and nucleosynthetic yield calculations of AGB and super-AGB stars[2], but they did not study models below $Z = 10^{-4}$. Campbell & Lattanzio (2008) presented primordial to extremely metal-poor star yields up to $3\,M_\odot$. Iwamoto (2009) computed the evolution and nucleosynthesis of intermediate-mass models at $Z = 2 \times 10^{-5}$. Cristallo et al. (2009, 2011, 2015) presented yields for low- and intermediate-mass stars in the metallicity range ($-2.15 \le$ [Fe/H] $\le +0.15$). Chieffi et al. (2001) and Abia et al. (2001) computed yields of primordial stars in a wide mass range (between low and massive). The evolution and nucleosynthesis in the poorly explored lowest-metallicity regime involve peculiar phenomena, such as double-shell and double-core flashes (Campbell & Lattanzio 2008), the corrosive second dredge-up (Gil-Pons et al. 2013; Doherty et al. 2014b), and the hot third dredge-up (Chieffi et al. 2001; Goriely & Siess 2004; Herwig 2004; Gil-Pons et al. 2013; Straniero et al. 2014), which definitely merit proper analysis.

From the point of view of observations of metal-poor stars relevant for the understanding of the evolution of the primitive universe, it is important to recall the amount of data from big surveys, such as the HK objective-prism survey (Beers et al. 1992), the Hamburg-ESO survey (Christlieb et al. 2002), SkyMapper (Keller et al. 2007), the Sloan Extension for Galactic Understanding and Exploration, SEGUE (Yanny et al. 2009), and the Large Sky Area Multi-Object Fibre Spectroscopic Telescope, LAMOST (Cui et al. 2012) to be further expanded as WEAVE (Dalton et al. 2012), the PRISTINE survey (Starkenburg et al. 2017), and especially with the James Webb Space Telescope (Zackrisson et al. 2011). At present almost 1000 stars with [Fe/H] $\lesssim -3$ have been detected in the Milky Way and dwarf galaxies. These tend to show high abundance dispersion, which reflects stochasticity in the nature of their progenitors: one CEMP star may show the signature of a single or very few stars, which makes them excellent laboratories to test early stellar nucleosynthesis.

The aim of this work is to address the problem of the scarcity of nucleosynthetic yield calculations in the EMP regime, to explore the effects of input physics, and to compare our theoretical results with observational data in the relevant metallicity regime. We present the yields of $Z = 10^{-5}$ stars of initial masses between 3 and $7.5\,M_\odot$, slightly overlapping the upper mass limit presented in Campbell & Lattanzio (2008) ($\le 3\,M_\odot$).

This manuscript also represents an extension of the work by Doherty et al. (2014a,b), in which the nucleosynthesis of massive AGB and Super-AGB stars from $Z = 10^{-4}$ to solar metallicity ($Z = 0.02$) was analysed. Part of the stellar structure calculations upon which this work is based were presented in Gil-Pons et al. (2013). In order to quantify the effect of the uncertain wind mass-loss rates, we include new models computed with an alternative mass-loss prescription, and postprocess all the stellar structure results with a nucleosynthesis code. We also explore the main trends of evolution and yields with metallicity in the metal-poor regime.

The results presented are of potential interest in the context of stellar archaeology (see e.g. Frebel & Norris 2015), because comparison between theoretical gas yields and observations of CEMP stars in the Halo and dwarf galaxies may provide insight into the chemistry of the early universe, and into the nature of the early stellar populations. Such comparisons can also help to constrain the uncertain input physics of CEMP stars, specifically those related to the efficiency of stellar winds. They could help us to understand the pollution history of the intracluster medium, and eventually the origin of multiple populations in globular clusters (Ventura et al. 2016). Used as inputs for Galactic chemical evolution (GCE) models, our yields can also help in understanding the chemical evolution of the early universe, and can be used to probe the Milky Way structure and formation history (Gibson et al. 2003). Our results can also be used as input physics for population synthesis in order to constrain the primitive IMF (Suda et al. 2013), and understand mass transfer in low- and intermediate-mass metal-poor stars (Abate et al. 2016).

This manuscript is organised as follows. Section 2 summarises the evolution of $Z = 10^{-5}$ IM EMPs, and describes trends with different wind prescriptions and metallicities. Section 3 analyses the nucleosynthesis and the evolution of surface abundances of our computed models. Section 4 presents our yields and production factors, Sect. 5 explores the trends with metallicity and input physics of yields computed here and others from the literature, and Sect. 6 presents a brief discussion of the binary channel for the formation of EMP stars, and a comparison to observational data. Finally, Sect. 7 summarises the main conclusions drawn from this study.

2. Summary of the structural evolution of intermediate-mass EMP models

We now briefly present the code and summarise the main results presented in Gil-Pons et al. (2013) in order to compare with the new calculations presented in this work. This new release includes a range of new models of initial masses between 3 and $7.5\,M_\odot$ computed with an alternative wind prescription during the AGB phase. Here, we also intend to emphasise the main characteristics of the evolution which ultimately determine the nucleosynthesis described in detail in the forthcoming sections.

2.1. Code and input physics description

Our nucleosynthetic calculations are the result of postprocessing on existing structure profiles computed with the Monash-Mount Stromlo code MONSTAR (Frost & Lattanzio 1996; Campbell & Lattanzio 2008), and presented in Gil-Pons et al. (2013, 2018). Its main characteristics involve the determination of convective boundaries using the Schwarzschild criterion, complemented with an attempt to search for neutrality (see, e.g. Castellani et al. 1971; Frost & Lattanzio 1996). The ratio of mixing-length to pressure scale height, α, was taken is 1.75.

---

[2] Super-AGB stars are those that undergo a C-burning phase prior to the thermally pulsing phase, the TP-(S)AGB; for a recent review see Doherty et al. (2017).

2.1.1. Mass loss

Mass-loss rates during the red giant branch (RGB) are set to follow the prescription by Reimers (1975). However, we note that mass loss in this part of the evolution is irrelevant at the considered initial metallicity (see Sect. 2.2). Mass-loss rates during the AGB or Super-AGB phases follow Vassiliadis & Wood (1993, hereafter VW93) These authors determined a direct relation between mass-loss rate and pulsation period from an analysis of CO microwave observations of AGB stars. To test the dependence of our results on this physical input, additional calculations are presented in this work, following Bloecker (1995, hereafter Blo95). The Blo95 formulation is based on the Reimers (1975) mass-loss rate, and considers atmospheric calculations for Mira stars made by Bowen (1988); it includes a parameter η to be determined by calibration. For instance, Ventura et al. (2000) proposed a value $\eta = 0.02$ based on observations of Li-rich giants in the Large Magellanic Cloud. This value for η was also used, for instance, by Ventura et al. (2001) and Doherty et al. (2014b). That of VW93 is the standard mass-loss prescription when MONSTAR (and similar versions of this code) is used. However, η values proposed by Reimers (1975) of between 5 and 10 were used by Karakas (2010) to compute $Z = 10^{-4}$ models, and with $\eta = 0.02$ proposed by Blo95 is more frequently considered by authors computing very low-Z models (e.g. Herwig 2004).

It is also commonly assumed that mass-loss rate depends on metallicity. Pauldrach et al. (1989) proposed a scaling relation of the form:

$$\dot{M}(Z_{\text{surf}}) = \left(\frac{Z_{\text{surf}}}{Z_\odot}\right)^n \dot{M}(Z_\odot),\tag{1}$$

where Z_{surf} is the stellar metal surface abundance, and n is an exponent typically ranging between 0.5 and 0.7. However, the arguments for this scaling relation were derived from line-driven winds, and are therefore relevant for more massive and hotter stars than the ones we are considering. The characteristic higher luminosity of low-Z stars, their surface C-abundances, pulsations, and their possibility to form dust might allow for wind mechanisms (and rates) not so different from those of higher Z stars (e.g. Mattsson et al. 2008; Lagadec & Zijlstra 2008). Therefore, we opted for not introducing any Z-scaling.

2.1.2. Opacities and initial composition

Interior stellar opacities are from Iglesias & Rogers (1996). We use low-temperature opacities that take into account composition changes in C, N, and O. It has been shown that this is critical in this metallicity range, both for the duration of the TP-AGB phase, and for the overall efficiency of nucleosynthesis and mixing during this stage (see Constantino et al. 2014). Low-temperature opacity tables are from Lederer & Aringer (2009) and Marigo & Aringer (2009).

Initial composition was solar scaled as in Grevesse & Noels (1993). EMP stars are known to have α-enhancements; however we opted for keeping continuity with the existing grid in Doherty et al. (2014a,b) and defer α-enhanced calculations to a future work. Only the isotopes relevant for the energy generation were considered in the stellar structure calculations (^{1}H, ^{3}He, ^{4}He, ^{12}C, ^{14}N, ^{16}O, and Z_{other}, which included all other species). Nuclear reaction rates were taken from Caughlan & Fowler (1988), and updated with NACRE (Angulo et al. 1999).

2.2. Evolution up to the TP-(S)AGB

The details of the evolution of intermediate-mass $Z = 10^{-5}$ stars were thoroughly described in Gil-Pons et al. (2013). Here we present a summary of the most relevant features for the nucleosynthesis, as well as additional sequences calculated both with the wind rate prescriptions by VW93, as in Gil-Pons et al. (2013), and with those by Blo95 with parameter $\eta = 0.02$, 0.04, and 1.

Our models experienced a pre-TP-(S)AGB evolution characteristic of IM EMPs of $Z \lesssim 10^{-5}$, with core H- and He-burning occurring before the first ascent of the giant branch and its associated dredge-up episode (Girardi et al. 1996; Chieffi et al. 2001). Our 7 and 7.5 $M_\odot$ models experience off-centre C-burning and eventually develop degenerate ONe cores surrounded by CO shells. This process is well known since the 1990s (see, e.g. Garcia-Berro & Iben 1994; Siess 2006; Gil-Pons et al. 2003; Doherty et al. 2010; Jones et al. 2013)

Models of initial mass M_{ini} between 3 and 6.5 $M_\odot$ experience a standard second dredge-up (SDU) episode during which the convective envelope advances inwards and reaches regions of the star previously processed by H-burning via the CN-cycle. More massive models undergo the corrosive SDU in which the base of the convective envelope advances even deeper, and reaches regions processed by He-burning. Given that our models do not include rotation, the first event to alter the surface composition is the (corrosive) SDU. Recall that stars of metallicity $Z = 10^{-5}$ do not experience a first dredge-up episode, but we keep the nomenclature SDU to refer to the dredge-up occurring during the early-AGB for consistency with the evolution of higher metallicity stars.

2.3. Evolution during the TP-(S)AGB

Metallicity influences the evolution of the TP-(S)AGB of intermediate-mass stars mainly through its effects on mass-loss rates and therefore on the duration of this phase. Figure 1 shows a summary of relevant parameters during the TP-(S)AGB stars of our $Z = 10^{-5}$ sequences, compared to $Z = 10^{-4}$ and $Z = 0.001$ sequences which were computed with similar versions of MONSTAR (see Sect. 2.1). We note that comparisons are not straightforward, as the input physics in these versions of the code present some relevant variations. VW93 mass-loss rates are used in all cases except our $Z = 10^{-5}$ models calculated with Blo95, and the $Z = 10^{-4}$ sequences by Karakas (2010), who used the prescription by Reimers (1975) corrected with a multiplying parameter η_R varying between 5 (for the 3 $M_\odot$ model), 7 (for the 4 $M_\odot$ model), and 10 (for models of $M_{\text{ini}} \geq 5 M_\odot$). Karakas (2010) also scaled mass-loss rates with metallicity as $\dot{M} = \sqrt{Z/Z_\odot}\, \eta_R \dot{M}_R$, where $\dot{M}_R$ represents the mass-loss rates exactly as in Reimers (1975). As we see below, these differences in wind prescriptions strongly affect the TP-AGB evolution and ultimately the nucleosynthetic yields.

2.3.1. Third dredge-up

All our models experience a third dredge-up (TDU) to varying extents. The efficiency of this process is described by the parameter $\lambda = \frac{\Delta M_{\text{dredge}}}{\Delta M_{\text{core}}}$, where ΔM_{dredge} is the H-exhausted core mass dredged-up by the convective envelope after a thermal pulse, and ΔM_{core} is the amount by which the core has grown during the
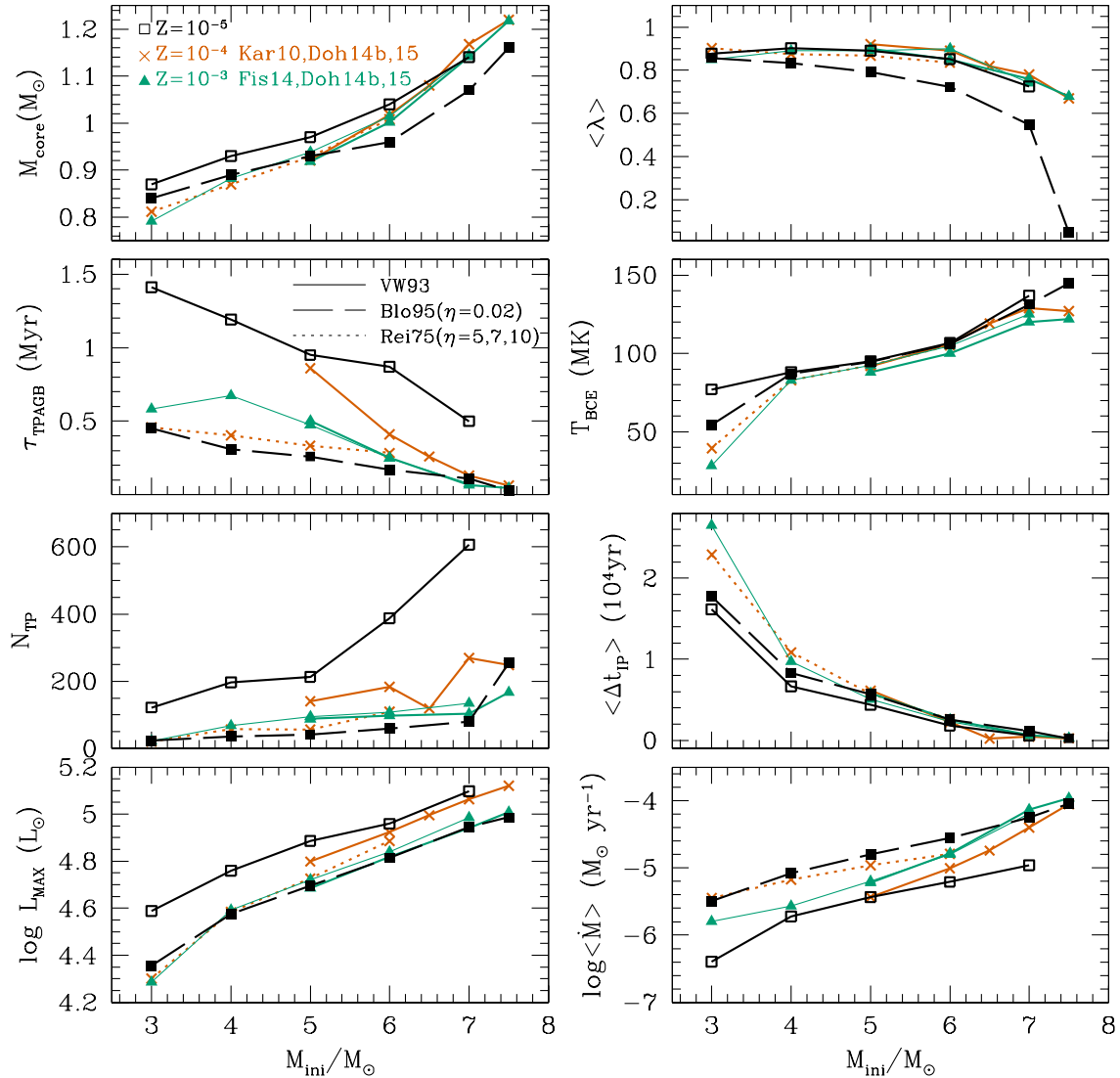
Fig. 1. Relevant TP-(S)AGB parameters for intermediate-mass models of different metallicities calculated with similar versions of the Monash-Mount Stromlo stellar evolution code. M_{core} is the core mass at the end of the TP-(S)AGB calculations, λ is the average TDU parameter, τ_{TPAGB} is the duration of the TP-(S)AGB phase, T_{BCE} is the maximum temperature at the base of the convective envelope, N_{TP} is the number of thermal pulses, t_{IP} is the average interpulse period, L_{MAX} is the maximum luminosity, and $\dot{M}$ is the average mass-loss rate during the TP-(S)AGB phase. Values are shown for our $Z = 10^{-5}$ models (black); for $Z = 10^{-4}$ models from Karakas (2010; dotted orange), and from Doherty et al. (2014b, 2015; solid orange); for $Z = 10^{-3}$ models for Fishlock et al. (2014; thin green) and Doherty et al. (2014b, 2015; thick green). Sequences calculated with the wind prescriptions by VW93, Reimers (1975), and Blo95 are shown, respectively, with solid, dotted and dashed lines.

previous interpulse period. λ tends to increase during approximately the first ten thermal pulses, and remains almost constant during the remaining TP-(S)AGB phase. This parameter is known to decrease with increasing mass (Straniero et al. 2003). The reason for this relationship is ascribed to the fact that more massive AGB stars have hotter and more compact cores. The temperature in the He-burning shell is higher, radiation pressure more important, and degeneracy consequently lower. These structural changes contribute to weaken the thermal pulses, and reduce both the duration of the instability and of the interpulse (for more details, see Siess 2010). Our models reproduce these trends, as seen in Table 1, and in Fig. 1. The most massive EMP stars ($M_{ini} \gtrsim 5-6\,M_\odot$) also experience hot TDU (Chieffi et al. 2001; Herwig 2004) during which the H-burning shell is not completely extinguished and maintains high luminosities (up to $10^4-10^5\,L_\odot$) during the thermal pulse. As a consequence, the advance inwards of the base of the convective envelope is

prematurely quenched. The effect of hot TDU can also be seen in Fig. 1, as $\langle\lambda\rangle$ values for the $Z = 10^{-5}$ models of initial mass $\gtrsim 5\,M_\odot$ tend to be lower than those of higher metallicity of analogous masses.

It should be stressed that the TDU efficiency strongly depends on the treatment of convective boundaries and specifically on the implementation of overshooting (see, e.g. Freytag et al. 1996). We note that the TDU efficiency decreases with increasing M_{ini} between $\lambda \sim 1$ and $\lambda \sim 0.05$. The latter low value corresponds to the $7.5\,M_\odot$ case computed with Blo95, which has a very short TP-SAGB phase. Some authors obtained significant TDU for their primordial to very metal-poor massive AGB and Super-AGB models (Chieffi et al. 2001; Herwig 2004; Lau et al. 2008; Karakas 2010; Gil-Pons et al. 2013), whereas others (Gil-Pons et al. 2003, 2005; Siess 2010; Suda & Fujimoto 2010) did not find any TDU. This issue is still controversial, particularly at the lowest metallicity regime.

Table 1. Main characteristics of the TP-(S)AGB of our $Z = 10^{-5}$ models.

$M_{\rm ini}$ $M_\odot$	$N_{\rm TP}$	$\tau_{\rm TP-(S)AGB}$ Myr	$\Delta t_{\rm IP}$ yr	$M_{c,\rm ini}$ $M_\odot$	$M_{c,f}$ $M_\odot$	$M_{\rm env,f}$ $M_\odot$	$\langle T_{\rm HeBS}\rangle$ MK	$\langle T_{\rm HBS}\rangle$ MK	$\langle T_{\rm BCE}\rangle$ MK	$M_{\rm dredge}^{\rm tot}$ $M_\odot$	$\langle\lambda\rangle$	$\langle\dot{M}_{\rm wind}\rangle$ $M_\odot$ yr^{-1}
VW93
3	122	1.41	16 148	0.81	0.87	0.10	345	83	68	0.70	0.98	4.0×10^{-7}
4	197	1.19	6702	0.87	0.93	0.25	359	91	85	0.53	0.92	1.9×10^{-6}
5	213	0.95	4382	0.91	0.97	0.54	357	95	88	0.40	0.91	3.7×10^{-6}
6	372	0.87	1828	0.98	1.04	0.69	362	104	99	0.36	0.85	6.2×10^{-6}
7	607	0.50	739	1.05	1.14	0.73	367	117	114	0.24	0.78	1.1×10^{-5}
Blo95
3	23	0.45	17 750	0.81	0.84	0.54	320	88	34	0.15	0.80	3.2×10^{-6}
4	35	0.31	8285	0.87	0.89	0.62	328	95	62	0.14	0.88	8.3×10^{-6}
5	43	0.26	5681	0.91	0.93	0.01	329	101	73	0.12	0.78	1.6×10^{-6}
6	60	0.17	2574	0.96	0.98	0.20	330	110	89	0.09	0.72	2.8×10^{-5}
6 ($\eta = 0.04$)	41	0.13	2523	0.96	0.98	0.01	319	112	84	0.002	0.66	3.9×10^{-5}
6 ($\eta = 1$)	16	0.03	2393	0.96	0.97	0.01	283	111	54	0.001	0.33	2.0×10^{-4}
7	82	0.11	1428	1.05	1.07	0.40	325	126	117	0.015	0.55	5.6×10^{-5}
7.5	254	0.06	423	1.13	1.16	0.42	300	146	142	0.005	0.01	9.1×10^{-5}

Notes. $M_{\rm ini}$ corresponds to the initial mass. $N_{\rm TP}$, $\tau_{\rm TP-(S)AGB}$, and $\Delta t_{\rm IP}$ are, respectively, the number of thermal pulses, the duration of the TP-(S)AGB (given from the first thermal pulse until the end of our computations), and the interpulse period. $M_{c,\rm ini}$, $N_{c,f}$ and $M_{\rm env,f}$ are, respectively, the masses of the H-exhausted cores prior to the TP-(S)AGB, and the masses of the H-exhausted cores and the remnant envelopes at the end of the TP-(S)AGB. $\langle T_{\rm HeBS}\rangle$, $\langle T_{\rm HBS}\rangle$, $\langle T_{\rm BCE}\rangle$ are, respectively, the temperatures at the times of maximum luminosity for each pulse, given at the centre of the He-burning shell, at the centre of the H-burning shell, and at the base of the convective envelope, and averaged over the number of thermal pulses in each sequence. $M_{\rm dredge}^{\rm tot}$ is the total mass dredged-up $\langle\lambda\rangle$ was also averaged over the number of thermal pulses in each case, and $\langle\dot{M}_{\rm wind}\rangle$ is the average mass-loss rates due to winds, that is, the envelope mass lost over the duration of the (S)AGB phase. Models were calculated using both the Vassiliadis & Wood (1993) and Bloecker (1995) with $\eta = 0.02$ mass-loss rate prescription. The 6 $M_\odot$ model includes additional calculations with $\eta = 0.04$ and $\eta = 1$. Some of the entries for models between 4 and 7 $M_\odot$, computed with VW93, were presented in Tables 1 and 3 of Gil-Pons et al. (2013). We show them here to facilitate comparison.

2.3.2. Hot bottom burning

We can also see in Fig. 1 that the maximum temperature of the base of the convective envelope ($T_{\rm BCE}$) tends to increase with decreasing metallicity. This is once more related to the behaviour of core masses, and to a lesser extent to the fact that lower metallicity models have lower C-abundances in their envelopes and therefore need higher temperatures to keep up the CN-reaction rates required to maintain hydrostatic equilibrium. In $Z = 10^{-5}$ models with $M_{\rm ini} \geq 4\,M_\odot$, the temperature at the base of the convective envelope exceeds $\gtrsim 30\,$MK, and hot bottom burning (HBB) sets in (see, e.g. Dell'Agli et al. 2018, and references therein). The same happens in our 3 $M_\odot$ VW93 model after ten thermal pulses. We note that HBB is extremely sensitive to metallicity, and particularly so in the stellar-mass range considered in this work.

All our models experience an overall increase in ^{12}C surface abundances, either during the corrosive SDU or early thermal pulses. Indeed, despite the relatively high temperatures at the BCE, ^{12}C is very efficiently replenished by TDU during the numerous thermal pulses. In addition, very short interpulse periods (Table 1 and Fig. 1) contribute to the formation of ^{14}N but do not lead to significant destruction of ^{12}C.

2.3.3. Effects of mass-loss rates

Mass-loss rates (which tend to decrease with decreasing metallicity) are the key factor determining the main differences between models in Fig. 1, that is, the variation in duration of the TP-(S)AGB and interpulse period.

Unfortunately, the mass-loss rate is very uncertain for the evolution and nucleosynthesis of TP-(S)AGB stars, especially

so in the low-Z regime (Gil-Pons et al. 2018 and references therein). EMP stars are more compact and hotter than higher metallicity stars of similar masses, and therefore yield very low mass-loss rates when using the prescription by VW93, (which depends strongly on stellar radius and has a negative dependence on effective temperature). As shown by Doherty et al. (2014b), using the prescription by Blo95 (with $\eta = 0.02$), which has a very strong dependence on surface luminosity, dramatically shortens the duration of the TP-(S)AGB phase of $Z = 10^{-4}$ stars with respect to the sequences calculated with VW93. When the $Z = 10^{-5}$ models are considered with the Blo95 prescription instead of that of VW93, the duration of the TP-(S)AGB is shortened by a factor of three in the 3 $M_\odot$ model, and a factor of five in the 7 $M_\odot$ model. The maximum surface luminosity during the TP-(S)AGB also decreases (see Fig. 1), because the cores have less time to grow as massive as in the VW93 case. Because the Blo95 prescription is based on the Reimers (1975) formulation, the behaviour of mass-loss rates with luminosity is very similar in models computed with these prescriptions. We note that the implementation of VW93, which includes a relatively strong dependence on the effective temperature yields considerably lower mass-loss rates in the most massive $Z = 10^{-5}$ cases, which are more compact and hotter than their higher Z counterparts. The cooler 7 and 7.5 $M_\odot$ of $Z = 10^{-4}$ and $Z = 10^{-3}$ computed with VW93 have average mass-loss rates similar to the $Z = 10^{-5}$ models of the same mass computed with Blo95.

Due to the shorter duration of the TP-(S)AGB in models computed with the wind prescription by Blo95, the number of thermal pulses and the amount of dredged-up matter during the TDU also decrease (see Table 1 and Fig. 1). The effect is naturally more dramatic when the parameter values $\eta = 0.04$ and 1 are used. In these cases, the duration of the TP-AGB is reduced
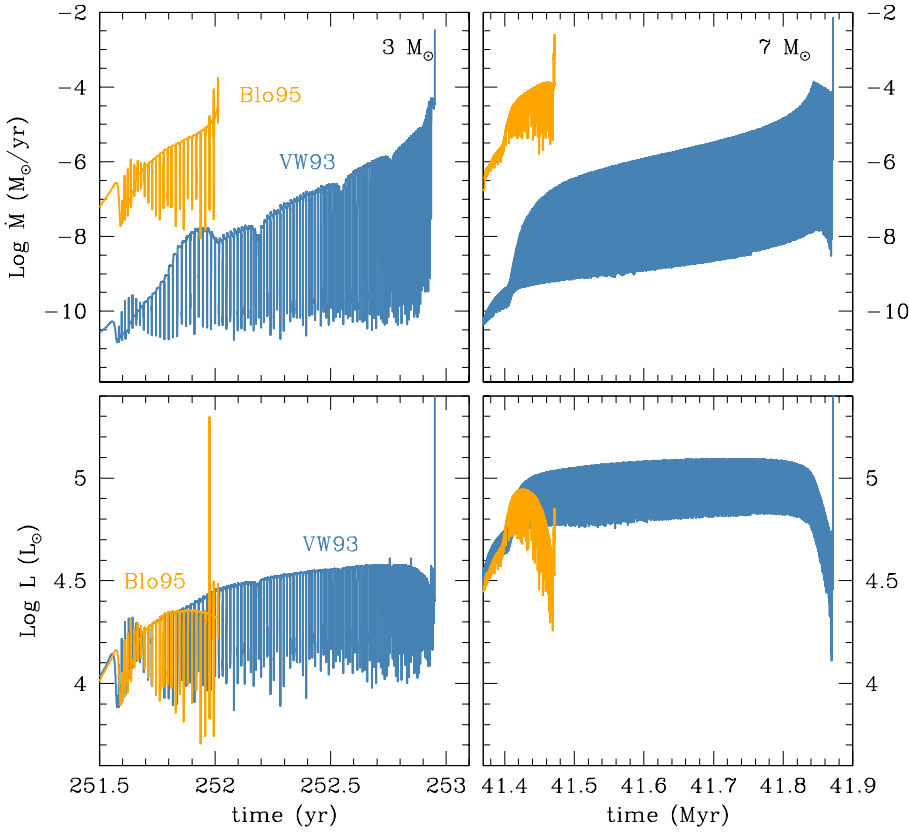
Fig. 2. *Left panels*: evolution of mass-loss rates (upper) and total luminosities (lower) for the $3\,M_\odot\,Z = 10^{-5}$ model computed with the prescriptions of Vassiliadis & Wood (1993; blue) and Bloecker (1995) with $\eta = 0.02$ (orange). *Right panel*: same for the $7\,M_\odot\,Z = 10^{-5}$ models.

by approximately a factor of 7 and 30 for the 3 and 7 $M_\odot$ models, respectively.

With increasing mass-loss rate, fewer TDU episodes occur and the surface enrichment is consequently reduced. As a result, the average efficiency $\langle\lambda\rangle$ is lower in our sequences calculated with Blo95 compared to those using the VW93 prescription (see Table 1 and Fig. 1). We also note that the rise in $\langle\lambda\rangle$ with thermal pulse number is almost independent of the mass-loss-rate prescription. The maximum efficiency is reached at about the same pulse number and its value is also highly comparable. We note finally that a shorter TP-(S)AGB phase leads to a lower HBB efficiency, because it operates over a shorter time and on top of a less massive core, which implies lower BCE temperatures. We can see from Fig. 1 that the effect of mass-loss rate on T_{BCE} is very mild between 4 and 7 $M_\odot$, but becomes significant for our lowest mass models. The 3 $M_\odot$ models are close to the lower mass threshold required for the occurrence of HBB, and therefore the model calculated with Blo95, which evolves rapidly on the TP-AGB, cannot develop an efficient HBB by the time most of its envelope is lost.

When considering the effects of mass-loss rate on the TP-AGB evolution at various metallicities (Fig. 1), we must recall that the mass-loss rates used for the $Z = 10^{-4}$ models are from those of Reimers (1975), and lead to considerably shorter TP-AGB phases than those resulting from the prescription by VW93. For a comparison, the $Z = 10^{-4}$, 5 $M_\odot$ model calculated with Reimers (1975) undergoes 69 thermal pulses, whereas the same model computed with VW93 undergoes 138 thermal pulses (see Karakas & Lattanzio 2007). As a consequence of the different wind prescription, the duration of the TP-AGB phase of $Z = 10^{-4}$ models becomes even shorter than that of $Z = 0.001$ of analogous masses.

The upper left panel of Fig. 1 shows that the initial-to-final mass relation of $Z = 10^{-5}$ models is less steep than that of higher

metallicity cases. Due to the significantly longer TP-AGB phases of $Z = 10^{-5}$ cases, the 3 and 4 $M_\odot$ models develop more massive cores than their higher Z counterparts, regardless of the wind prescription. We also note that faster evolving super-AGB models ($M_{ini} \gtrsim 7\,M_\odot$) yield very similar final core masses that are almost independent of metallicity when the same (VW93) prescription is used. The use of Blo95, which leads to even faster evolution, yields final cores with masses that are between 0.03 and 0.08 $M_\odot$ lower.

In summary, due to the SDU and early TP-(S)AGB evolution, the metallicity (in terms of Z) is increased to near-solar, and the subsequent TP-(S)AGB evolution of our initially EMP models is qualitatively very similar to that of metal-rich stars. However, it is interesting to note some relevant quantitative differences. Compared to higher metallicity models, EMP stars have:

– longer duration of the TP-(S)AGB, determined mainly by the relative weakness of winds at lower metallicity;
– shorter interpulse periods Δt_{IP} as a consequence of their larger core masses;
– a higher number of thermal pulses (both because of the shorter Δt_{IP} and the longer duration of the TP-(S)AGB);
– thinner intershell masses;
– higher convective intershell temperatures ($\gtrsim 360$ MK);
– higher temperatures at the base of the convective envelope (average $T_{BCE} \gtrsim 33$ MK).

We finally note that just like metal-rich stars, model convergence is lost prior to the complete ejection of the H-rich envelope (remnant envelope mass may be as high as $\gtrsim 1\,M_\odot$ for our more massive models). This failure is related to the development of an Fe-opacity peak near the base of the convective envelope, and was analysed in Lau et al. (2012). It is also interesting to note that the remaining envelope mass at the end of our calculations is lower when higher wind rates are used. Indeed, the instability
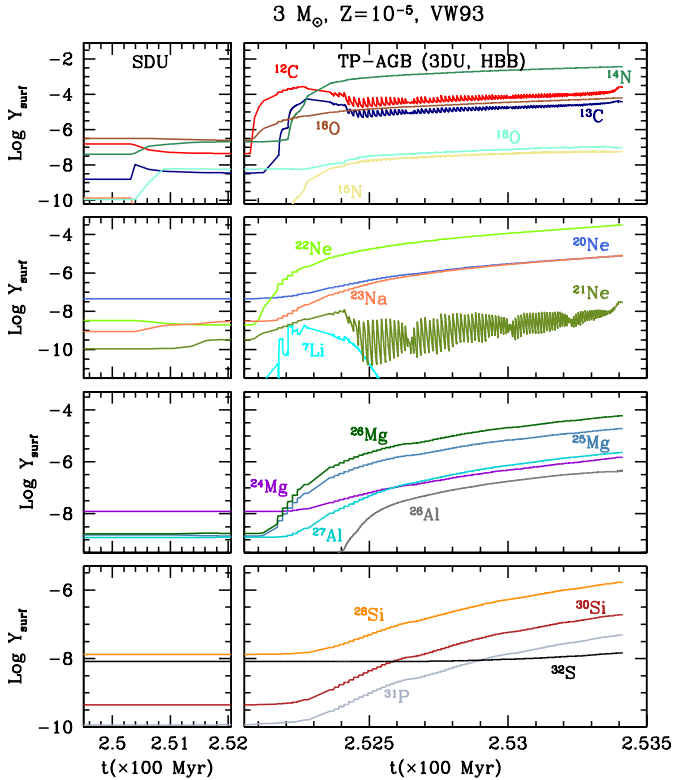
Fig. 3. Evolution of the surface abundances of some selected isotopes for the $3\,M_\odot\,Z = 10^{-5}$ model computed with the Vassiliadis & Wood (1993) mass-loss rates.
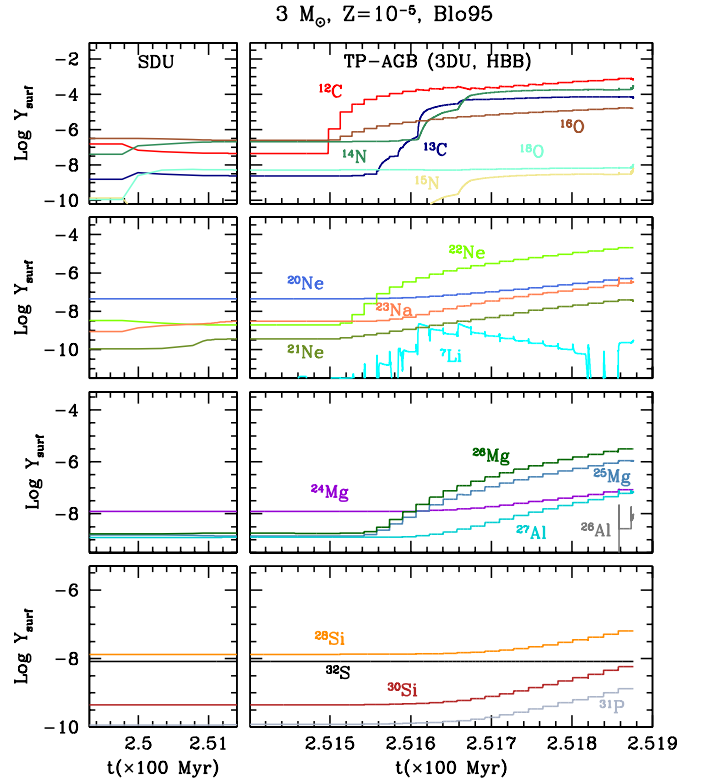
Fig. 4. Evolution of the surface abundances of some selected isotopes for the $3\,M_\odot\,Z = 10^{-5}$ model using mass-loss rates as in Bloecker (1995); see main text for details.

described in Lau et al. (2012) seems to be favoured by the higher density and temperature at the BCE which are achieved in models with slower mass-loss rates (and thus more massive final H-exhausted core). The immediate evolution of the star after this instability remains a subject of debate.

3. Nucleosynthesis and evolution of isotopic surface abundances

3.1. Code description

Detailed nucleosynthetic calculations were performed using MONSOON, the postprocessing code developed at Monash University (Cannon 1993; Lugaro et al. 2004; Doherty et al. 2014a). MONSOON takes the basic structure profiles of the models computed with MONSTAR (temperature, density, convective velocity at each mass point) as inputs. It calculates abundance variations due to nuclear reaction rates and time-dependant convection using a "donor cell" scheme (Cannon 1993; Henkel et al. 2017). MONSOON builds its own mesh-point distribution for each new model, which allows higher resolution in regions with large abundance variations.

Nuclear reaction rates are mostly from the JINA reaction library (Cyburt et al. 2010). p-captures for the NeNa-cycle and MgAl chain are from Iliadis et al. (2001), p-captures on ^{22}Ne are from Hale et al. (2002), α-captures on ^{22}Ne are from Karakas et al. (2006), and p-captures on ^{23}Na are from Hale et al. (2004). The version of MONSOON used for the present work includes 77 species, up to ^{32}S and Fe-peak elements. Additionally, it includes a "g" particle (Lugaro et al. 2004), which is a proxy for s-process elements. Eventual neutron captures on nuclides, which are not present in our network, are accounted for by assigning a cross-

section to n-captures on ^{62}Ni which corresponds to an average of cross-sections of n-captures up to ^{209}Bi. This neutron-sink approach was used by Jorissen & Arnould (1989), Lugaro et al. (2003), and Herwig et al. (2003).

We note that the use of a postprocessing code does not allow the feedback of detailed composition on the evolution. The effects on the equation of state (through the mean molecular weight), energy generation and on the opacities are however expected to be very limited because we are dealing with trace elements.

3.2. Surface composition changes during the standard and corrosive second dredge-up

During a standard SDU a very strong surface enrichment in ^{4}He abundance, $X_{\rm surf}(^4{\rm He})$, occurs. Our models have an initial $X_{\rm surf}(^4{\rm He}) = 0.248$. In the case of our $3\,M_\odot$ model computed with VW93, $X_{\rm surf}(^4{\rm He}) = 0.277$ after the SDU, and 0.308 at the end of the evolution. Surface ^{4}He enhancement is even higher for more massive models. For our $6\,M_\odot$ model, $X_{\rm surf}(^4{\rm He})$ values at the end of the SDU and at the end of the evolution are, respectively, 0.339 and 0.373. Because the SDU is so efficient at increasing the surface ^{4}He, models computed with Blo95 also produced high yields of this isotope, in spite of their shorter TP-AGB. This is one of the main reasons why IM stars can be considered as good candidates for the pollution of the intracluster medium that gave rise to the formation of multiple stellar populations in globular clusters that are characterised by different He over-abundances (see, e.g. Milone et al. 2012, 2014; Piotto et al. 2012, 2013). We note also that helium mass fractions close to 0.4 have been reported (e.g. Norris 2004; Piotto et al. 2007; Bellini et al. 2013). The effects of SDU on isotopes beyond ^{4}He
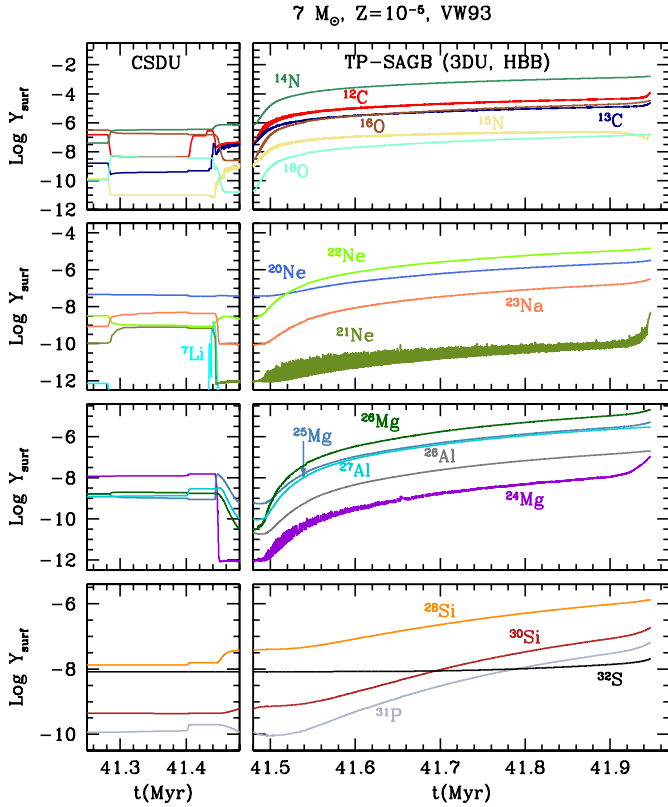
Fig. 5. Evolution of the surface abundances of some selected isotopes for the $7 M_\odot$ $Z = 10^{-5}$ model computed with the mass-loss rates by Vassiliadis & Wood (1993).
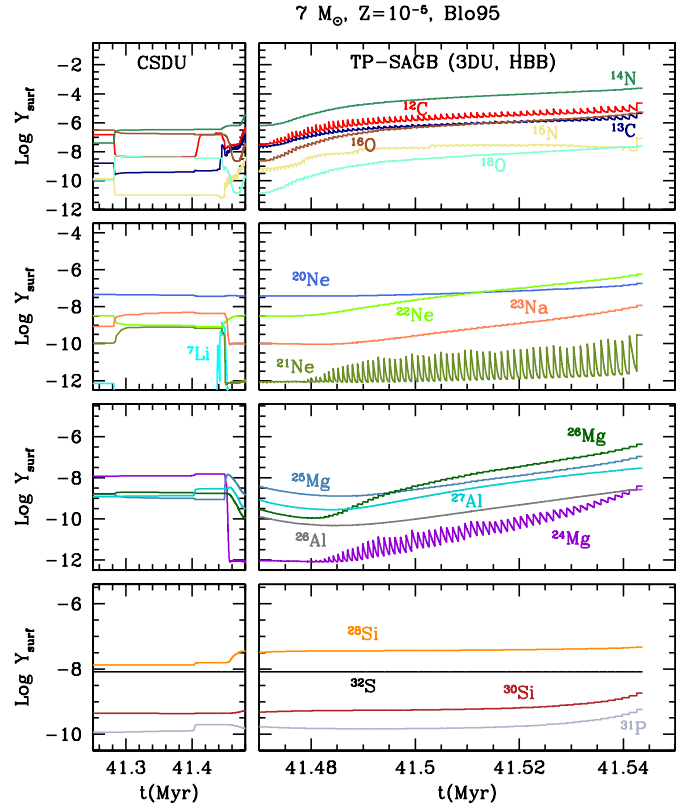
Fig. 6. Evolution of the surface abundances of some selected isotopes for the $7.5 M_\odot$ $Z = 10^{-5}$ model computed with the mass-loss rates by Bloecker (1995).

are also significant. Regardless of the wind prescription, ^{14}N surface abundances at the end of this episode increase by a factor of between five and six with respect to their initial values. Surface abundances of ^{18}O are moderately enhanced, as are those of ^{21}Ne and ^{23}Na but to a lesser extent. Simultaneously, ^{12}C is depleted and the abundances of ^{16}O and ^{22}Ne slightly decreased (Figs. 3 and 4).

Models of initial mass $M_{\rm ini} \gtrsim 7 M_\odot$ undergo the corrosive SDU (CSDU). Like normal SDU, CSDU causes a high increase in He (e.g. $X_{\rm surf}(^4{\rm He})$ is 0.364 at the end of the CSDU, and 0.456 at the end of the evolution of our model computed with VW93). In addition, mild enhancements occur for ^{13}C, ^{22}Ne (through ^{14}N$(\alpha,\gamma)^{18}$F$(\beta^+,\nu)^{18}$O$(\alpha,\gamma)^{22}$Ne), ^{23}Na, and ^{27}Al (see Figs. 5 and 6). Interestingly surface $X_{\rm surf}(^7{\rm Li})$ is clearly enhanced. It is created by e-capture on ^{7}Be which is itself formed by α-capture on ^{3}He (Cameron & Fowler 1971). Shortly afterwards, ^{7}Li is destroyed by p-captures. The distinctive signature of the CSDU is the additional pollution with He-burning products, mainly ^{12}C, which contributes to increasing the envelope opacity and in turn the mass loss rate (see, e.g. Marigo & Girardi 2007; Nanni 2018).

3.3. Nucleosynthesis during the TP-(S)AGB evolution

3.3.1. Third dredge-up episode

The TDU allows the transport to the surface of isotopes synthesised in the convective zones associated with thermal pulses. All our models experience TDU, the efficiency of which, as shown in Sect. 2, decreases with increasing initial mass (see Table 1). The TDU raises $X_{\rm surf}(^{12}{\rm C})$ by three orders of magnitude for the $3 M_\odot$ model calculated with VW93 (which reaches $X_{\rm surf}(^{12}{\rm C}) = 10^{-3}$)

and by two orders of magnitude for the $5 M_\odot$ model calculated with VW93 (up to $X_{\rm surf}(^{12}{\rm C}) = 2 \times 10^{-4}$).

The enhancements in ^{4}He and ^{12}C are the most significant signatures of the occurrence of TDU, but He-burning in the pulse-driven convective zone also contributes to the synthesis of ^{12}C(α,γ). To a lesser extent, ^{16}O also forms via ^{13}C$(\alpha,$n$)^{16}$O and ^{13}N$(\alpha,$p$)^{16}$O, and ^{20}Ne is slightly produced by ^{16}O$($n$,\gamma)^{17}$O$(\alpha,$n$)^{20}$Ne. Besides, ^{21}Ne is created through ^{16}O$($n$,\gamma)^{17}$O$(\alpha,\gamma)^{21}$Ne and ^{20}Ne$($n$,\gamma)^{21}$Ne. ^{22}Ne forms from ^{14}N$(\alpha,\gamma)^{18}$F$(\beta^+,\nu)^{18}$O$(\alpha,\gamma)^{22}$Ne. ^{25}Mg and ^{26}Mg are synthesised via $(\alpha,$n$)$ and (α,γ) reactions on ^{22}Ne, respectively. It is important to recall that in IM EMP stars, the H burning shell remains active during the development of the thermal pulse, with luminosities up to 10^4–$10^5 L_\odot$. This allows ^{4}He, ^{13}C, ^{14}N and ^{15}N to be created above the He-flash-driven convective zone while flashes are occurring. We note however that, because the H-burning and He-burning regions are not mixed until the subsequent TDU episode occurs, the matter synthesised in the H-burning shell cannot fuel He burning during the current flash. Neutrons, relevant for the occurrence of s-process nucleosynthesis, are produced mainly via ^{22}Ne$(\alpha,$n$)^{25}$Mg (Straniero et al. 1997) within the thermal pulse if the temperature at the base of the pulse exceeds $\gtrsim 3.5 \times 10^8$ K. This source is activated in our most massive $Z = 10^{-5}$ models. Right panels of Figs. 3–6 show the evolution abundances of selected isotopes during the TP-(S)AGB phase.

3.3.2. Hot bottom burning

The temperature at the base of the convective envelopes of our model stars is between 30 MK and $\gtrsim 140$ MK, and therefore their

TP-AGB phase is mostly dominated by the occurrence of HBB, in particular by the onset of the CN and NeNa-cycles and the MgAl chain. However, we note that, as mentioned above, our lowest $M_{\rm ini}$ case (3 $M_\odot$) does not develop significant HBB until its envelope has been sufficiently enriched in metals ($Z_{\rm env} \lesssim 10^{-3}$) due to efficient early TDU episodes (see Figs. 3 and 4).

From the nucleosynthetic point of view, the main result of HBB is an enrichment of the stellar envelope in ^{4}He (which was also enhanced by SDU). The onset of the CN-cycle also produces a significant increase in ^{14}N and ^{13}C, and milder enhancements in ^{15}N, at the expense of ^{12}C, ^{16}O, and ^{18}O. Despite the occurrence of HBB, overall the surface abundances of ^{12}C and ^{16}O reach near equilibrium values and even increase along the TP-(S)AGB phase because of the efficient TDU replenishing these isotopes. Also, the surface ^{12}C/^{13}C ratio remains nearly constant around its equilibrium value of 4 during most of the TP-(S)AGB evolution, and all our stars become C-rich.

Through the NeNa cycle, the surface abundance of ^{20}Ne increases at the expense of ^{21}Ne, ^{22}Ne, and ^{23}Na abundances. Because $T_{\rm BCE}$ values are higher (and therefore the NeNa cycle more efficient) for more massive models, ^{20}Ne enhancement is more significant. This can be seen by comparing Figs. 3 and 5. ^{21}Ne is quickly destroyed by p-capture during HBB, regardless of the initial mass. ^{22}Ne is converted into ^{20}Ne (^{22}Ne(p,γ)^{23}Na(p,α)^{20}Ne), and into ^{26}Mg by α-captures. However, ^{22}Ne is efficiently replenished by TDU raising its surface abundance and feeding the NeNa cycle. The implementation of the fastest Blo95 mass-loss rate decreases the time during which the NeNa cycle is active. It also reduces the number of TDU episodes, the final core mass, and incidentally $T_{\rm BCE}$. As a consequence, the enhancement of ^{23}Na and all the Ne isotopes is significantly diminished. This can be seen by comparing Figs. 3 and 4, which show the surface abundance evolution of 3 $M_\odot$ models with VW93 and Blo95 respectively, and by comparing Figs. 5 and 6, which show analogous information for the 7 $M_\odot$ cases.

The temperatures at the BCE are also high enough for the activation of the MgAlSi chain. ^{26}Al, ^{27}Al and ^{27}Si increase at the expense of Mg isotopes via proton captures and β-decays (^{24}Mg(p,γ)^{25}Al(β^+,ν)^{25}Mg(p,γ)^{26}Al(p,γ)^{27}Si(β^+,ν)^{27}Al). The higher the initial mass (and therefore the average $T_{\rm BCE}$), the higher the Al and Si yields. We note that these isotopes are relevant for the formation of grains and can ultimately impact stellar wind. As it happens with the NeNa cycle, the shorter TP-(S)AGB duration and lower $T_{\rm BCE}$ of Blo95 models significantly reduce the yields of all the isotopes involved in the MgAlSi chain. It is important to recall that, given the high $T_{\rm BCE}$ values of our models, uncertainties in the rates of the reactions involved in the NeNa cycle and in the MgAlSi chain are expected to have an important effect on the corresponding nucleosynthetic yields (Izzard et al. 2006), especially those of ^{22}Ne, ^{23}Na, and ^{26}Al.

With higher mass-loss-rate prescriptions, the effect of HBB is reduced mainly because of the shorter duration of the TP-(S)AGB phase. The enrichment in ^{14}N and to a less extent of ^{13}C and ^{18}O are smaller. Specifically, both TDU and HBB act for shorter times, significantly reducing the surface enhancement of all isotopes above ^{20}Ne with respect to the cases computed with VW93. We also note that ^{12}C is only weakly affected by the different wind prescriptions because its abundance is maintained at its equilibrium value. Figures 3 and 4 show the effect of different mass-loss rates on the surface abundance evolution of the most abundant isotopes.

4. Nucleosynthetic yields

Net nucleosynthetic yields of isotope i are expressed in $M_\odot$ and calculated as follows:

$$M_i = \int_0^{t_{\rm end}} [X_i(t) - X_{i,{\rm ini}}] \dot{M}(t){\rm d}t, \tag{2}$$

where $t_{\rm end}$ is the time at the end of our calculations, $X_{i,{\rm ini}}$ is the initial mass fraction of isotope i, $X_i(t)$ its value at an arbitrary time t, and $\dot{M}(t)$ is the mass-loss rate at t.

As mentioned in Sect. 2.3, due to the occurrence of an opacity-related instability, some envelope mass is left at the end of our calculations. The further evolution of stars at this point is unknown, and they might either recover stability and proceed along some more thermal pulses, or quickly eject their remaining envelopes. We assume the latter happens, and the corresponding contribution to the yields is calculated by assuming no further nuclear processing, that is, by substracting the mass of each isotope in the remaining envelope minus the mass of that isotope that a remaining envelope of the same mass and initial composition would have.

The expected abundances associated to the ejected matter are presented in Table A.1 and in Fig. 7. The most striking feature in this figure points to the key role of the highly uncertain mass-loss rates in this metallicity regime. As described in Sect. 3, all our models produce significant amounts of He, C, and N due to the combination of HBB and TDU. Models computed with the VW93 mass-loss treatment experience longer TP-(S)AGB phases and longer (and more efficient) CNO, NeNa, and MgAl processing as well as more dredge-up episodes. As a consequence, their abundance patterns (in terms of their ejecta) for elements between Ne and P are one to two orders of magnitude higher than those of their analogous cases calculated with Blo95. We note in addition the trend with initial masses. In general, lower mass models (which also experience longer TP-(S)AGB phases) yield higher abundances.

Detailed yield tables, together with mass lost, initial and average abundances, and production factors for each of our 77 species are presented in the Supplementary Information in the same format as Doherty et al. (2014a,b) and available online[3] and at the CDS.

The production factor for each species, i, is defined as

$$P_i = \log \frac{\langle X_i \rangle}{X_{i,{\rm ini}}}, \tag{3}$$

where $\langle X_i \rangle = \frac{1}{t_{\rm star}} \sum_{j=1}^{N} X_{ij}(t)\Delta t_j$ with $t_{\rm star} = \sum \Delta t_j$ is the age of the star, Δt_j is the duration of time step j, and $X_{ij}(t)$ is the surface abundance of isotope i at that time. Figure 8 compares production factors for EMPs and very metal-poor models of different initial masses. We include the results from our work, as well as the $Z = 10^{-4}$ models of Karakas (2010) and Doherty et al. (2014b), and the $Z = 0.001$ models by Fishlock et al. (2014) and Doherty et al. (2014b). The overproduction factors show the effects of the TDU and HBB nucleosynthesis described in detail in Sect. 3. Specifically, these figures highlight the increasing efficiency of TDU and HBB for decreasing metallicity. For instance, the production factors of ^{15}N, ^{17}O, and ^{21}Ne are negative for the $Z = 10^{-3}$ 5 and 7 $M_\odot$ models, and positive otherwise. This is because in metal poor stars the initial isotopic abundances are lower, the temperature of nuclearly active layers is hotter, the dredge-up efficiency is higher, and the duration of their TP-(S)AGB phase is longer.
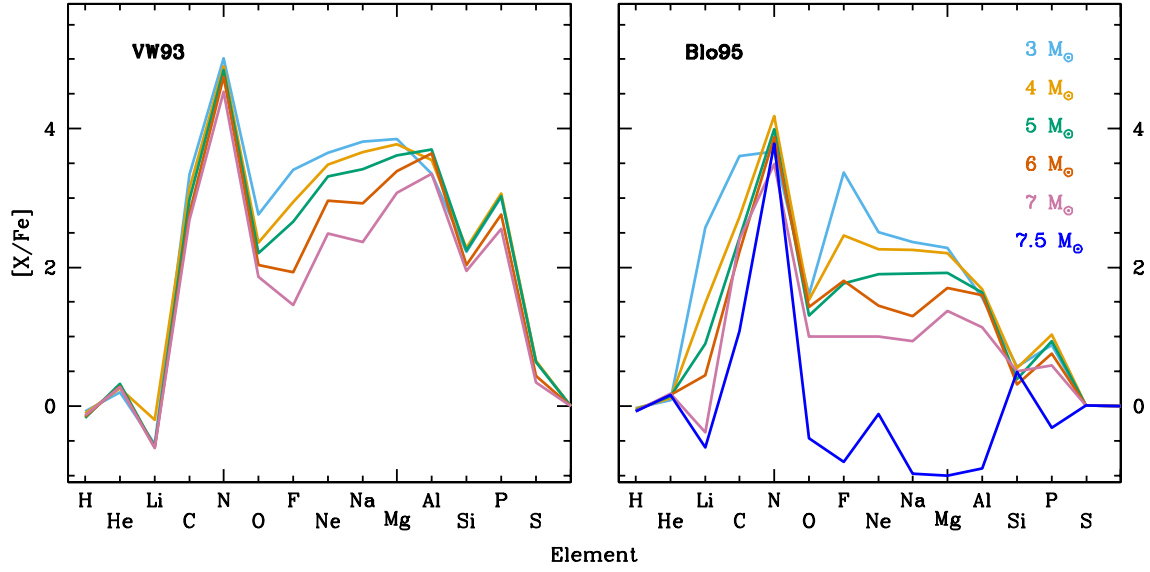
Fig. 7. Abundance pattern in terms of the ejecta of our models in the [X/Fe] notation. Solid lines refer to models computed with VW93, and dashed lines refer to those computed with Blo95.
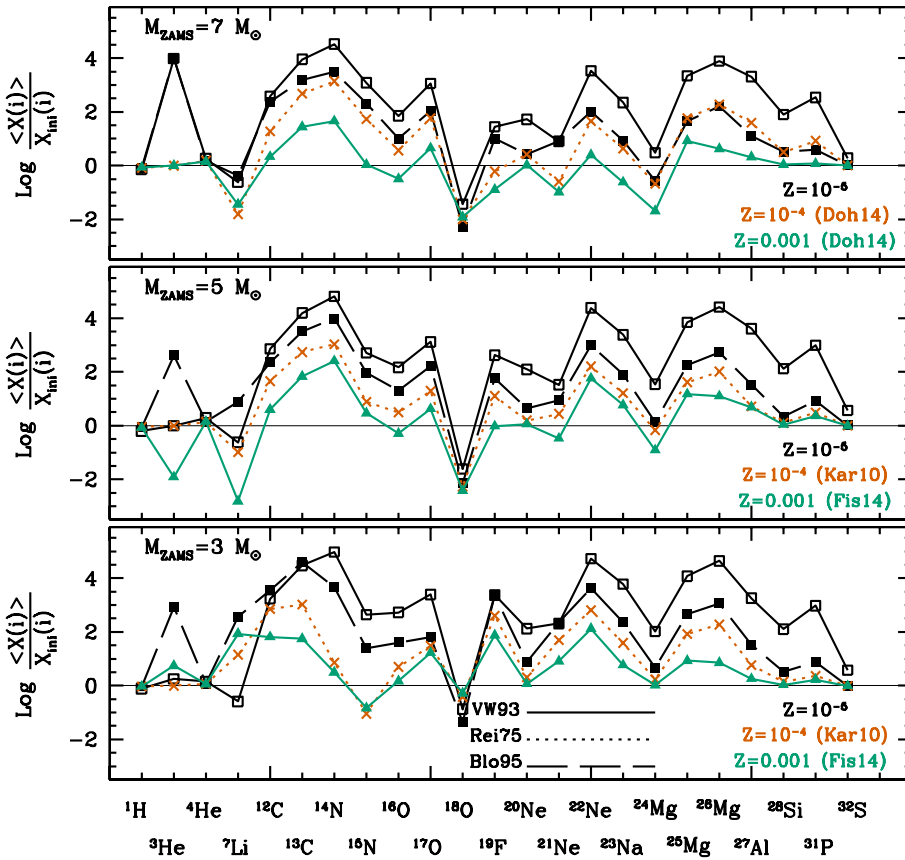

Fig. 8. Production factor of selected isotopes for the low metallicity models of 7, 5, and 3 $M_\odot$. The $Z = 10^{-5}$ results (black) are compared with the $Z = 10^{-4}$ calculations (orange) of Karakas (2010) for the 3 $M_\odot$ and 5 $M_\odot$ cases, and Doherty et al. (2014b) for the 7 $M_\odot$. Results are also compared with the $Z = 0.001$, 3, and 5 $M_\odot$ models by Fishlock et al. (2014) and with the 7 $M_\odot$ model by Doherty et al. (2014b). All models were calculated with the same Vassiliadis & Wood (1993) wind prescription (VW93), except for the ones shown with dotted and dashed lines, which were calculated with Reimers (1975; Rei75) and Bloecker (1995) with $\eta = 0.02$ (Blo95).

As explained in Sect. 3, with a higher mass-loss rate (Blo95), the TP-(S)AGB is considerably shortened and the TDU and HBB efficiencies lower, and so the production factors are generally reduced with respect to the calculations by VW93. However, ^{12}C yields are practically the same with Blo95, as the abundance of this isotope is maintained at its equilibrium value. ^{3}He and ^{7}Li production factors also increase, both for the 3 $M_\odot$ and the 5 $M_\odot$ models calculated with Blo95. ^{7}Li is produced during HBB through the Cameron-Fowler mechanism (Cameron & Fowler

1971), but is easily destroyed (through ^{7}Li(p,α)α at temperatures as low as 3.5 MK. Models computed with Blo95 destroy ^{7}Li less efficiently because of the relative shortness of their evolution.

Lithium abundance analysis is considered an important diagnosis tool for the understanding of globular cluster chemical enrichment processes (D'Orazi et al. 2014) although, as pointed out by Ventura & D'Antona (2010), from the theoretical point of view, its nucleosynthetic yields are strongly affected by
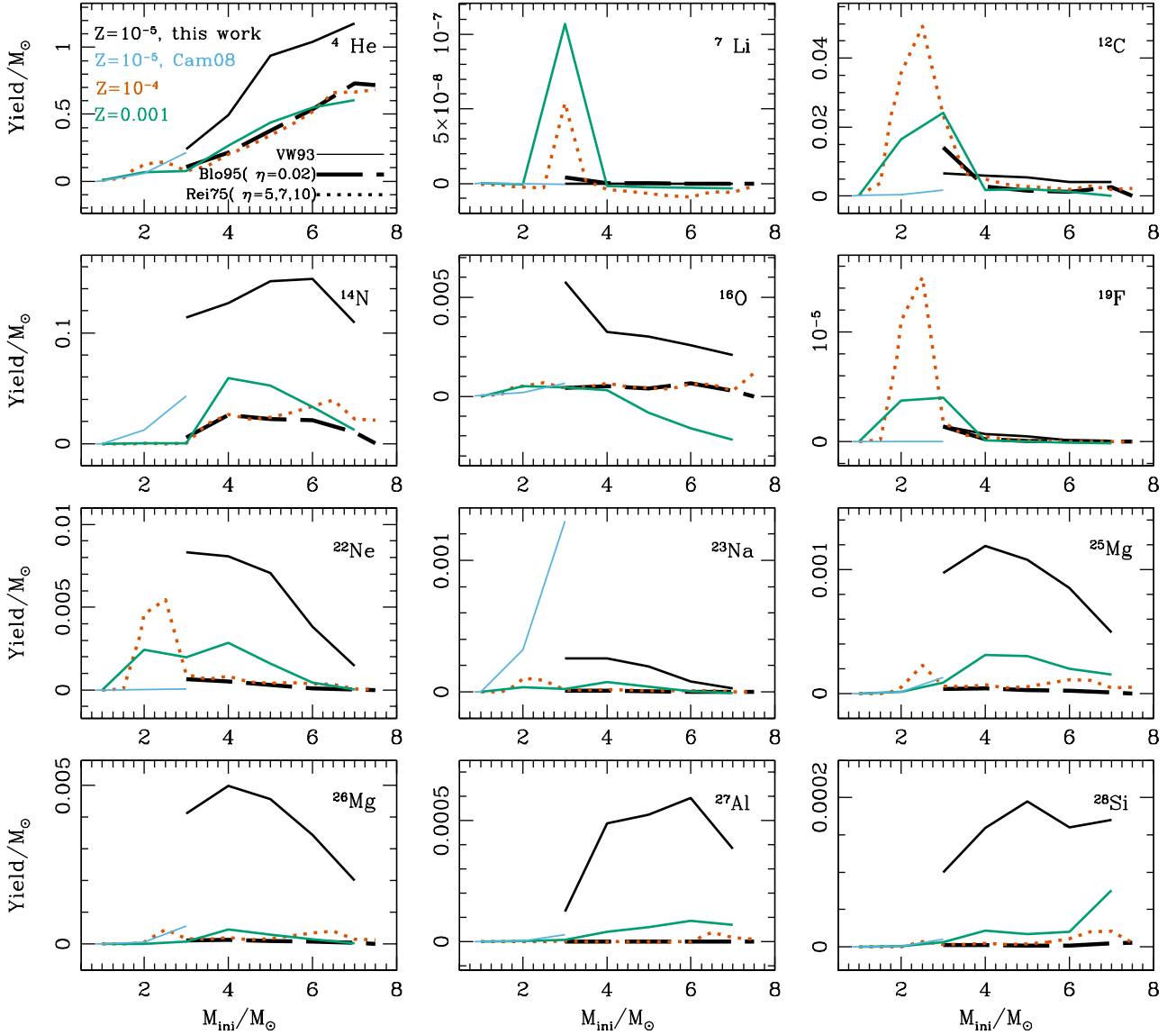
Fig. 9. Yields of intermediate-mass stars of different metallicities. Values for $Z = 10^{-5}$ cases are shown in thin blue lines for the models calculated with VW93 from Campbell & Lattanzio (2008; 0.85, 1, 2 and 3 $M_\odot$). Our models computed with VW93 (between 3 and 7 $M_\odot$) are shown in black solid lines, and those with Blo95 are shown in black dashed lines. Values in orange correspond to the $Z = 10^{-4}$ models from Karakas (2010; 1 to 6 $M_\odot$) and (Doherty et al. 2014b; 7 and 7.5 $M_\odot$). Values in green correspond to the $Z = 10^{-3}$ models from Fishlock et al. (2014; 1 to 6 $M_\odot$) and Doherty et al. (2014b; 7 and 7.5 $M_\odot$).

uncertainties on input physics. Specifically, the behaviour of ^{7}Li could be relevant for the understanding of multiple-population low-mass globular clusters, as many of them show Li production and furthermore have first- and second-generation stars which share very similar Li abundances (see, e.g. M12 in D'Orazi et al. 2014, or NGC 362 in D'Orazi et al. 2015, and references therein).

For the sake of comparison, let us recall that the FRUITY database (Cristallo et al. 2015) also includes the detailed nucleosynthesis yields of intermediate-mass models of $Z = 10^{-4}$. These authors used the wind rates proposed by Straniero et al. (2006) and introduced an α enhancement which was not present in the calculations by Karakas (2010), and directly affect the yields of these elements. In addition, HBB in the FRUITY models is less efficient than in Karakas (2010). Ritter et al. (2018) compared NuGrid model yields with those from Herwig (2004), Karakas (2010), and FRUITY. These authors pointed out a coincidence of results within a factor of two or three, and justified yield differences on the bases of convective boundary mixing prescriptions and resolution affecting the treatment of HBB.

5. Preliminary exploration of the implications on Galactic chemical evolution

As mentioned in Sect. 1, there are no detailed nucleosynthetic yields of intermediate-mass stars of $Z \lesssim 10^{-5}$ in the literature apart from the work by Iwamoto (2009). Given the uncertainties in the input physics in this metallicity regime, and its critical effects on the yields, the possible effects of $Z = 10^{-5}$ intermediate-mass stars on GCE are poorly known. In this section we compile our results and those obtained with similar versions of the codes described in Sects. 2 and 3. Specifically, in Fig. 9 we present our yields for the isotopes with the highest production factor values (see also Fig. 8), and compare these

to the $Z = 10^{-4}$ cases from Karakas (2010) and Doherty et al. (2014b), and the $Z = 0.001$ models by Fishlock et al. (2014) and Doherty et al. (2014b). We also include the yields from the $Z = 10^{-5}$, 0.85, 1, 2, and 3 $M_\odot$ models by Campbell & Lattanzio (2008).

Figure 9 further illustrates the strong effect of the mass-loss-rate prescriptions (recall that all models use the prescription by VW93, except the additional set of $Z = 10^{-5}$ models computed with Blo95, and the $Z = 10^{-4}$ models, which use Reimers 1975). As different wind prescriptions cause higher variations in yields than metallicity effects, it is difficult to determine clear trends with metallicity. Compared to higher metallicity cases, $Z = 10^{-5}$ models computed with VW93 globally produce significantly higher yields of ^{4}He, ^{14}N, ^{16}O, ^{22}Ne, the heavy Mg isotopes, ^{27}Al, and ^{28}Si. Specifically, such high ^{14}N production, which is already expected in AGB stars of [Fe/H] $\gtrsim -2.5$ (Vincenzo et al. 2016; Kobayashi et al. 2020), may help explain observations of EMP stars (see, e.g. Spite et al. 2006). The production of ^{27}Al and ^{28}Si may impact the formation of dust that drives the winds of intermediate-mass EMP stars. As a reference, our $Z = 10^{-5}$ models (computed with the prescription by VW93) dredge-up a total amount of matter that is between five and eight times higher than the $Z = 10^{-4}$ cases by Karakas (2010), which were computed with the fast winds provided by Reimers (1975) with $\eta = 5, 7, 10$. Yields of isotopes that tend to reach equilibrium values (such as ^{12}C), or that are very fragile, such as ^{7}Li and ^{19}F, increase in the mass range 2–4 $M_\odot$ when efficient winds are considered. One could expect that, if the $Z = 10^{-4}$ models had been computed with the less efficient prescription by VW93, the associated yields would be between the $Z = 10^{-5}$ and the $Z = 0.001$ cases displayed. We also note the great similarly between the $Z = 10^{-4}$ yields of Karakas (2010) and the $Z = 10^{-5}$ ones using Blo95.

Understanding the evolution of the yields at $Z = 10^{-5}$ between the 0.85 and 3 $M_\odot$ models of Campbell & Lattanzio (2008), and those computed here is nearly impossible given the significant differences in input physics. Campbell & Lattanzio (2008) used the Schwarzschilds criterion for convective boundaries, which yields inefficient or no TDU at all, and also used constant composition low-temperature opacities, which strongly impact the mass-loss rate (Marigo 2002). In addition, nuclear reaction rates during the post-processing calculations were different. Campbell & Lattanzio (2008) considered the REACLIB data, which are based on a 1991 update of the compilation by Thielemann et al. (1986; see Lugaro et al. 2004), whereas we used the new rates described in Sect. 3.1. This is expected to significantly affect yields of isotopes involved in the NeNa cycle and the MgAl chain, and especially ^{23}Na yields (Karakas 2010). These differences in the input physics introduce strong discontinuities in the yield of a given element as a function of initial mass as can be seen in Fig. 9.

The actual contribution of our model stars to Galactic chemical evolution would depend on the IMF which, unfortunately, is poorly known at the EMP metallicty regime. We note that the primitive IMF might not be as strongly biased towards low masses as the present-day initial mass function, IMF, (see e.g. Salpeter 1955; Miller & Scalo 1979, or Kroupa 2001). Suda et al. (2013) suggested that the Galactic IMF might have undergone a transition from massive star to low-mass star dominated at [Fe/H] ~ -2. If this were the case, the contribution to the Galactic chemical inventory of our model stars (above 3 $M_\odot$) might be higher than expected from standard IMFs.

When looking at the Li abundances (Table A.1) we can see that most lie in the range of observed values ($0 \lesssim \log \epsilon_{obs}(\text{Li}) \lesssim$
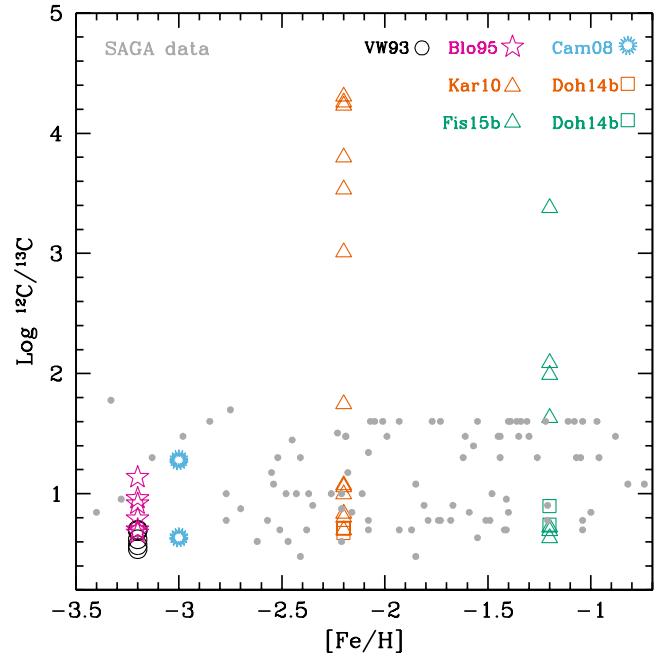
Fig. 10. Averaged carbon isotopic ratios vs. metallicity resulting from our model stars using the VW mass-loss prescription (black circles), and Blo95 with $\eta = 0.02$ (pink stars); from Campbell & Lattanzio (2008; blue stars); Karakas (2010; orange triangles), Doherty et al. (2014b; orange squares); Fishlock et al. (2014; green triangles), and from Doherty et al. (2014b; green squares). Grey symbols represent the observed ratios obtained from the SAGA database (Suda et al. 2008).

2.8), and only our 3 $M_\odot$ case computed with Blo95 lies above the Spite plateau (log ϵ(Li) = 2.2). In general, the lowest mass models yield higher log ϵ(Li), because the temperatures at the base of the convective envelope of the former are lower. We note however that the mass-loss-rate prescription is, again, critical for the $Z = 10^{-5}$ models, as those computed with Blo95 allow the removal of most of the convective envelope before ^{7}Li abundances substantially decrease (see Ventura & D'Antona 2010 for further discussion).

Comparison between theoretical results and observationally determined isotopic ratios has proven to be an important tool for Galactic chemical evolution, as different isotopes of the same element may be formed through different processes or in stars of different initial masses (see, e.g. Kobayashi et al. 2011; Romano et al. 2017). When considering the results of intermediate-mass models, isotopic ratios of ^{12}C/^{13}C are useful to determine the relative importance of TDU (which efficiently transports ^{12}C) and HBB (which destroys ^{12}C and produces ^{13}C at the base of the convective envelope in AGB stars of initial mass $\gtrsim 3$–4 $M_\odot$). ^{12}C is also significantly produced in massive stars (Kobayashi et al. 2011), and ^{13}C might also be produced in fast-rotating massive stars (see, e.g. Meynet & Maeder 2002; Chiappini et al. 2008). In order to illustrate how massive AGB and Super-AGB stars contribute to this isotopic ratio as a function of metallicity, we present in Fig. 10 the resulting ratio patterns in terms of the ejecta of ^{12}C and ^{13}C, for metal-poor models between $Z = 10^{-5}$ and $Z = 0.001$, and compare them with data from the SAGA database (Suda et al. 2008). Unfortunately, the number of observations for [Fe/H] $\lesssim -2.5$ is small. We note that the [Fe/H] $= -3.2$ and [Fe/H] $= -3$ models cover the range of observations reasonably well (except, perhaps, for the highest mass and the VW93 cases), and account for the observed spread in ^{12}C/^{13}C.

Magnesium is another of the few elements for which isotopic ratios may be determined (see, e.g. Gay & Lambert 2000; Yong et al. 2003; Meléndez & Cohen 2009; Agafonova et al. 2011). Comparisons between GCE models and observations have been used for example to constrain star formation rates on cosmological timescales (Vangioni & Olive 2019), to determine the onset of the contribution of AGB stars to GCE (Fenner et al. 2003; Meléndez & Cohen 2007), to establish the timescale for the formation of the Galactic halo (Carlos et al. 2018), or to understand self-enrichment in globular clusters (Ventura et al. 2018). All three stable magnesium isotopes can be formed in both massive and intermediate-mass stars, however massive stars are not able to produce the heavier isotopes ^{25,26}Mg in significant amounts (see Timmes et al. 1995; Alibés et al. 2001), as opposed to low-metallicity AGB stars (Karakas & Lattanzio 2003). Fenner et al. (2003) concluded that GCE models need to include metallicity-dependant AGB yields in order to reproduce Mg isotopic ratios observations for [Fe/H] < −1. Meléndez & Cohen (2007) added additional metal-poor stars to the sample of Mg isotopic ratio observations and compared to GCE models to establish that AGB stars did not contribute to the Galactic halo until metallicities [Fe/H] ≳ −1.5. Vangioni & Olive (2019) recently confirmed that AGB stars are the main contributors to the heavy Mg isotopes, and that the agreement between models and observations down to [Fe/H] = −2.5 improves when intermediate-mass stars are considered, especially if their mass range is restricted to masses between 5 and 8 $M_\odot$.

As expected, our $Z = 10^{-5}$ models produce massive amounts of the heavy Mg isotopes compared to ^{24}Mg, especially when the less efficient wind rates by VW93 are used. For instance, the relation ^{24}Mg:^{25}Mg:^{26}Mg is 1:27:113 for our 5 $M_\odot$ model computed with VW93, and 1:18:60 for the model of the same initial mass computed with Blo95. The 7.5 $M_\odot$ model computed with Blo95, which has a very short TP-SAGB phase, yields a Mg isotopic relation 1:12:10. The $Z = 10^{-4}$ 5 $M_\odot$ model by Karakas (2010) also has Mg isotopic ratios favouring the heavy isotopes: 1:8:23. As a reference, observed ^{25,26}Mg/^{24}Mg ratios tend to decrease with metallicity, which attests an early production of ^{24}Mg by massive stars. However, we note that there are very few determinations of Mg isotopic ratios below [Fe/H] = −2, and no observation at all below [Fe/H] = −2.5. We expect that future campaigns will go beyond this threshold. Comparison between GCE models and observations of Mg isotopic ratios might be used to further constrain input physics, such as the elusive stellar wind rates in EMP IM stars, just as they helped to constrain rotation in massive models (Vangioni & Olive 2019).

6. A binary scenario for the formation of EMP stars

To assess the possibility that our model stars are the evolved companions of currently observed CEMP stars, we revisited the analysis developed in Gil-Pons et al. (2013), based on the binary formation scenario proposed by Suda et al. (2004). Observed CEMP stars have low masses (≲1 $M_\odot$), and provided the initial orbital period is long enough, the low-mass secondary is able to accrete a fraction of the wind material ejected during the TP-(S)AGB phase of the companion and avoid common envelope evolution.

Low-mass EMP stars have a very thin convective envelope, but hydrodynamical processes such as thermohaline mixing (see, e.g. Kippenhahn et al. 1980; Chen & Han 2004; Stancliffe et al. 2007) can induce further dilution of the accreted material in the (S)AGB companion. In particular, Stancliffe et al. (2007) proposed that the accreted material could be mixed throughout
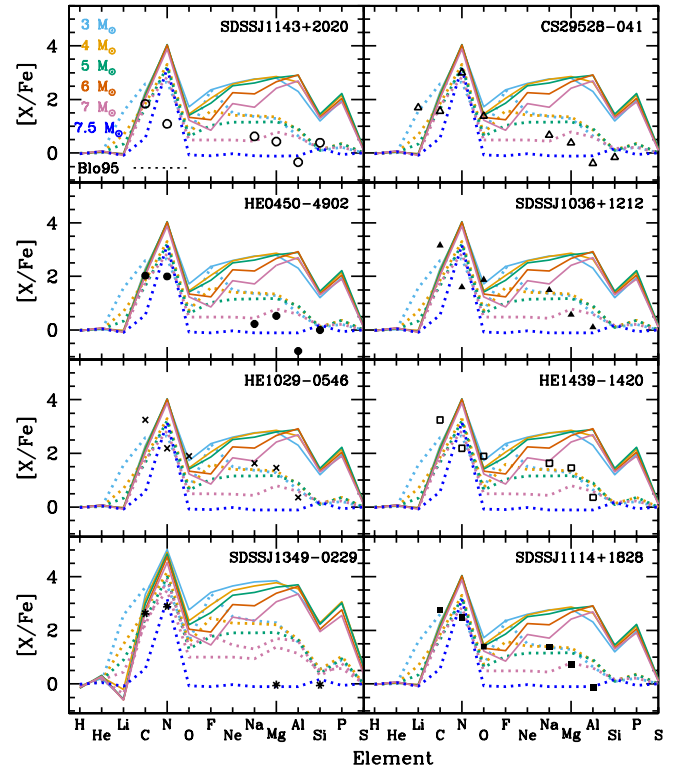
Fig. 11. Abundance pattern in terms of the ejecta of selected elements. These values correspond to a hypothetical case in which 1% of the matter ejected by our evolved models is homogeneously mixed in the 0.2 $M_\odot$ envelope of an unevolved low-mass $Z = 10^{-5}$ star (see main text for justification). Black symbols correspond to observed abundances of selected CEMP-s stars from the SAGA database Suda et al. (2017). Models computed with Vassiliadis & Wood (1993) and with Bloecker (1995) are shown, respectively, in solid and dotted lines.

90% of the low-mass accretor. However, we note that the efficiency of this mechanism was questioned by Aoki et al. (2008), who observed that CEMP turn-off and red giants present very different [C/H] abundances. According to these latter authors, this suggests the absence of efficient mixing prior to the red giant phase. Denissenkov & Pinsonneault (2008) analysed the observed variations of [C/H] and [N/H] in the surface of CEMP stars that had undergone the first dredge-up. These latter authors showed that assuming a binary scenario in which the matter transferred from the evolved star was mixed throughout the uppermost 0.2 $M_\odot$ layers of its unevolved companion leads to theoretical surface abundances that are in good agreement with the observational results. The theoretical explanation for the loss of efficiency of thermohaline mixing might be related to the effect of gravitational settling (Stancliffe et al. 2009).

Following this idea, we calculated new abundance patterns associated to the dilution of 1% of our ejecta in the uppermost 0.2 $M_\odot$ of a low-mass EMP star of the same initial metallicity. These new abundances are shown in Table A.1 (see Appendix A). For comparison, we also display in Fig. 11 the expected abundance pattern in terms of the ejecta from our diluted models, together with the observed abundances of the eight main sequence N-rich CEMP-s stars of the Galactic halo which host the highest surface N abundances (we note that our model stars produce large amounts of this element), with metallicity in the range −3.6 < [Fe/H] < −2.9, that is, within a 0.3 dex interval around our initial composition ([Fe/H] = −3.2, which corresponds to $Z = 10^{-5}$). Abundances
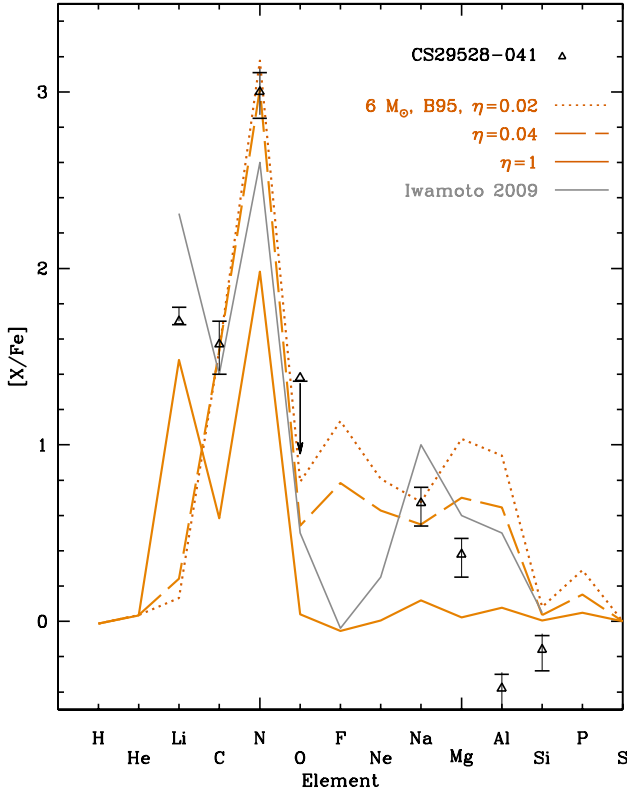
Fig. 12. Abundance pattern in terms of the ejecta of the $6\,M_\odot$ models computed with the Blo95 wind prescription, and assuming dilution with a low-mass star envelope (see Fig. 11 and main text for details), with $\eta = 0.02$, (dotted line), $\eta = 0.04$ (dashed line), and $\eta = 1$ (solid line). Abundances from the $Z = 2 \times 10^{-5}$, $6\,M_\odot$ model by Iwamoto (2009) are shown by the grey solid line. Symbols represent the observed abundances of CS29528-041.

were taken from the SAGA database (Suda et al. 2008, 2011, 2017; Yamada et al. 2013), which refer to the following publications for each individual object: Sivarani et al. (2006) for CS29258-041, Behara et al. (2010) for SDSSJ1349-0229, Spite et al. (2013) for SDSSJ1114+1828 and SDSSJ1143+2020, Cohen et al. (2013) for HE1439-1420, and Hansen et al. (2015) for HE0450-4902 and HE1029-0546. We note that, in general, agreement between model and observations improves when the wind prescription by Blo95 is used, with the possible exception of the ^{12}C/^{13}C ratio.

The high N and C abundances of CS29258-041 suggest a progenitor undergoing both HBB and TDU, and therefore its abundances might be better explained using intermediate-mass models like ours. Sivarani et al. (2006) themselves compared their observational data with the yields from a $6\,M_\odot$ model of metallicity [Fe/H] $= -2.3$ computed by Herwig (2004). This model gives [C/Fe] $= 1.2$ and [N/Fe] $= 2.3$. By comparison, our $6\,M_\odot$ model computed with the Blo95 ($\eta = 0.02$) mass-loss rates yields higher CN abundances with [C/Fe] $= 2.23$ and [N/Fe] $= 3.88$ (see Table A.1 in Appendix A). When the parameter $\eta = 1$ is used along with Blo95, we obtain [C/Fe] $= 1.17$ and [N/Fe] $= 2.67$. We also note that the initial metallicity of the model by Herwig (2004) was $Z = 0.0001$, and so their comparison is rather artificial. Figure 12 shows our best fit to the observed objects of Fig. 11. For this comparison, we used our $6\,M_\odot$ model calculated with the wind prescription by Blo95 (and $\eta = 0.02$), under the assumption of dilution with a low-mass star envelope. We also show the results by Iwamoto (2009), who also

compared the yield abundances of his $Z = 2 \times 10^{-5}$ $6\,M_\odot$ model, computed with Blo95 and $\eta = 0.1$ to the observed abundances of CS29258-041. The match is reasonably good for the abundances of C, N, and O (although only an upper limit for the latter was given). Our Na abundance also appears within the error bar limits, but our model overproduces Mg by approximately 1 dex, Si by 0.5 dex, and especially Al, by almost 2 dex. We performed additional calculations with higher mass-loss rates, with the aim being to shorten the TP-AGB phase, and therefore HBB (and MgAl chain) responsible for the high overproduction of Al. Elements of mass equal to or above that of O show abundances approximately equal to solar, and thus the model still overproduces Al and Si with respect to the observed abundances of CS329528-041.

AGB models are not the only option proposed to explain the surface abundances of CS29528-041. Sivarani et al. (2006) also suggested that metal-poor massive stars with rotationally induced mixing could reproduce simultaneously high amounts of N and C (Hirschi et al. 2006; Meynet et al. 2006; Chiappini et al. 2006). However, a recent work (Choplin et al. 2017) shows that massive rotating models tend to overproduce Na and Mg unless one can assume that only the matter above the He-rich shell is ejected during the supernova explosion. This hypothesis would be analogous to the underlying assumptions of the faint supernovae scenario (Umeda & Nomoto 2005), and would work similarly to the wind-only enrichment proposed by Meynet et al. (2006) and Hirschi (2007). As Choplin et al. (2017) point out, a possible way to distinguish AGB and massive rotating star scenarios for the formation of EMP stars could involve the analysis of the ratio of light to heavy s-elements, which tend to be negative for AGBs (Abate et al. 2015), and positive for massive rotating stars (Cescutti et al. 2013).

We also explored the possibility that our extremely metal-poor models could match observations of stars from ultra-faint dwarf galaxies, as they are the most metal-poor objects known and, as such, are expected to be the least evolved (Simon 2019). The surface N-abundances of these objects were always below [N/Fe] $= 1.5.(\pm 0.5)$, and therefore we could not expect a reasonable match with our models, in which HBB plays such an important role. Therefore, additional comparative analysis is not given, and we defer further considerations until the sample of observations of objects of ultra-faint dwarf galaxies increases, or until binary model yields (which could remove HBB) are calculated.

7. Summary and discussion

We present the evolution and nucleosynthesis of stellar models with $Z = 10^{-5}$ and masses between 3 and $7.5\,M_\odot$, and compare them to models computed with similar versions of the Monash stellar evolution code (MONSTAR). Determining the trends of relevant evolutionary parameters with metallicity is not straightforward because of the lack of fully consistent input physics sequences amongst the models (e.g. variations in mass-loss rates, determination of convective boundaries, and low-temperature opacities). In terms of evolution, the most remarkable trend with decreasing Z is the longer duration of the TP-(S)AGB phase which, together with the shorter interpulse periods, leads to a higher number of thermal pulses. The use of different (and very uncertain) wind prescriptions affects these characteristics even more significantly than metallicity.

Nucleosynthesis in $Z = 10^{-5}$ massive AGB and Super-AGB stars is governed by the efficiency of both HBB and TDU. The former is a consequence of the high temperatures at the BCE, which allow the onset of the NeNa cycle and the MgAl chain. The trend to produce significant yields of ^{4}He and ^{14}N due to

HBB is shared by very massive AGB and Super-AGB stars of any metallicity. Specifically, the high ^{4}He yields produced by these model stars make them good candidates to pollute the intracluster medium and thus they may be key to understanding multiple populations of globular clusters.

Even though there is no consensus on the subject, and the dependency on input physics is very strong, the TDU efficiency of massive AGB and Super-AGB stars seems to be maintained for lower metallicities, at least down to $Z \sim 10^{-5}$. As a consequence of deep TDUs, all the $Z = 10^{-4}$ and $Z = 10^{-5}$ models display positive yields of ^{12}C and ^{16}O. In addition, because of the high temperatures achieved in the HeBS and the BCE, the heavy Mg isotopes also present positive yields. As shown by Siess (2010) and Doherty et al. (2014b), $Z = 10^{-4}$ models of massive AGB and Super-AGB stars produced large amounts of ^{13}C and ^{27}Al. $Z = 10^{-5}$ stars of analogous masses present even higher production factors for these isotopes and, unlike their $Z = 10^{-4}$ counterparts, produce positive (although low) yields of ^{21}Ne, ^{24}Mg, and ^{32}S.

The presented yields point to the potential relevance of our models as contributors of ^{4}He and ^{14}N, regardless of the wind prescription used. If real mass-loss rates are biased to low values, our sequences would also contribute to ^{16}O, ^{22}Ne, heavy Mg isotopes, ^{27}Al, and ^{28}Si, although the production of ^{16}O and ^{28}Si is mostly due to massive stars. More specifically, the yields of all the isotopes mentioned above are about one order of magnitude higher when computed with VW93 than when computed with Blo95 (with $\eta = 0.02$). These differences would impact Galactic chemical evolution models. In terms of isotopic ratios of ^{12}C/^{13}C and ^{25,26}Mg/^{24}Mg, the effects of the mass-loss rates are also crucial. We suggest that, once future observations of ^{25,26}Mg/^{24}Mg extend below [Fe/H] $= -2.5$, they could provide a useful tool to help constrain mass-loss rates in the EMP regime. The crucial effects of different wind prescriptions on the stellar yields presented hampers the detection of a clear trend with metallicity, and emphasise the importance of using consistent grids of nucleosynthetic yields as inputs for GCE models.

Comparison of yields from IM EMPs with nitrogen-rich CEMP-s stars from the Galactic halo is promising and should be considered for further study. Our models provide a better match to observations when the mass-loss rates by Blo95 with $\eta = 0.02$ – more efficient than those of VW93 – are used. The uncertain physics of mixing, possibly affected by magnetic buoyancy (Nucci & Busso 2014), gravity waves (Denissenkov & Herwig 2003; Battino et al. 2016), and rotation (Herwig 2005; Straniero et al. 2015; Cristallo et al. 2015), also plays a determining role in the evolution and yields, and its effects should be explored.

The environment where $Z = 10^{-5}$ stars formed show the specific signature of one or a few individual objects, rather than the mixture of a large number of stellar yields. Therefore, it is important to increase the number of observational counterparts, and perform a detailed exploration of extended nucleosynthesis (including s-process), and of the parameter space of theoretical models, probably combining both the initial compositions corresponding to the yields of primordial objects and the yields of our early generation models. Specifically, the effects of stellar winds, which prove to be critical for model results at the considered metallicity range, should be consistently taken into account.

References

Abate, C., Pols, O. R., Izzard, R. G., & Karakas, A. I. 2015, A&A, 581, A22
Abate, C., Stancliffe, R. J., & Liu, Z.-W. 2016, A&A, 587, A50
Abia, C., Domínguez, I., Straniero, O., et al. 2001, ApJ, 557, 126
Agafonova, I. I., Molaro, P., Levshakov, S. A., & Hou, J. L. 2011, A&A, 529, A28
Alibés, A., Labay, J., & Canal, R. 2001, A&A, 370, 1103
Angulo, C., Arnould, M., Rayet, M., et al. 1999, Nucl. Phys. A, 656, 3
Aoki, W., Beers, T. C., Sivarani, T., et al. 2008, ApJ, 678, 1351
Battino, U., Pignatari, M., Ritter, C., et al. 2016, ApJ, 827, 30
Beers, T. C., & Christlieb, N. 2005, ARA&A, 43, 531
Beers, T. C., Preston, G. W., & Shectman, S. A. 1992, AJ, 103, 1987
Behara, N. T., Bonifacio, P., Ludwig, H.-G., et al. 2010, A&A, 513, A72
Bellini, A., Piotto, G., Milone, A. P., et al. 2013, ApJ, 765, 32
Bloecker, T. 1995, A&A, 297, 727
Bowen, G. H. 1988, ApJ, 329, 299
Brusadin, G., Matteucci, F., & Romano, D. 2013, A&A, 554, A135
Cameron, A. G. W., & Fowler, W. A. 1971, ApJ, 164, 111
Campbell, S. W., & Lattanzio, J. C. 2008, A&A, 490, 769
Cannon, R. C. 1993, MNRAS, 263, 817
Carlos, M., Karakas, A. I., Cohen, J. G., Kobayashi, C., & Meléndez, J. 2018, ApJ, 856, 161
Cassisi, S., & Castellani, V. 1993, ApJS, 88, 509
Castellani, V., Giannone, P., & Renzini, A. 1971, Ap&SS, 10, 340
Caughlan, G. R., & Fowler, W. A. 1988, At. Data Nucl. Data Tables, 40, 283
Cescutti, G., Chiappini, C., Hirschi, R., Meynet, G., & Frischknecht, U. 2013, A&A, 553, A51
Chen, X., & Han, Z. 2004, MNRAS, 355, 1182
Chiappini, C., Matteucci, F., & Gratton, R. 1997, ApJ, 477, 765
Chiappini, C., Hirschi, R., Meynet, G., et al. 2006, A&A, 449, L27
Chiappini, C., Ekström, S., Meynet, G., et al. 2008, A&A, 479, L9
Chieffi, A., Domínguez, I., Limongi, M., & Straniero, O. 2001, ApJ, 554, 1159
Choplin, A., Hirschi, R., Meynet, G., & Ekström, S. 2017, A&A, 607, L3
Christlieb, N., Wisotzki, L., & Graßhoff, G. 2002, A&A, 391, 397
Cohen, J. G., Christlieb, N., Thompson, I., et al. 2013, ApJ, 778, 56
Constantino, T., Campbell, S., Gil-Pons, P., & Lattanzio, J. 2014, ApJ, 784, 56
Côté, B., West, C., Heger, A., et al. 2016, MNRAS, 463, 3755
Cristallo, S., Piersanti, L., Straniero, O., et al. 2009, PASA, 26, 139
Cristallo, S., Piersanti, L., Straniero, O., et al. 2011, ApJS, 197, 17
Cristallo, S., Straniero, O., Piersanti, L., & Gobrecht, D. 2015, ApJS, 219, 40
Cui, X.-Q., Zhao, Y.-H., Chu, Y.-Q., et al. 2012, Res. Astron. Astrophys., 12, 1197
Cyburt, R. H., Amthor, A. M., Ferguson, R., et al. 2010, ApJS, 189, 240
Dalton, G., Trager, S. C., Abrams, D. C., et al. 2012, in Ground-based and Airborne Instrumentation for Astronomy IV, Proc. SPIE, 8446, 84460
Dell'Agli, F., García-Hernández, D. A., Ventura, P., et al. 2018, MNRAS, 475, 3098
Denissenkov, P. A., & Herwig, F. 2003, ApJ, 590, L99
Denissenkov, P. A., & Pinsonneault, M. 2008, ApJ, 679, 1541
Doherty, C. L., Siess, L., Lattanzio, J. C., & Gil-Pons, P. 2010, MNRAS, 401, 1453
Doherty, C. L., Gil-Pons, P., Lau, H. H. B., Lattanzio, J. C., & Siess, L. 2014a, MNRAS, 437, 195
Doherty, C. L., Gil-Pons, P., Lau, H. H. B., et al. 2014b, MNRAS, 441, 582
Doherty, C. L., Gil-Pons, P., Siess, L., Lattanzio, J. C., & Lau, H. H. B. 2015, MNRAS, 446, 2599
Doherty, C. L., Gil-Pons, P., Siess, L., & Lattanzio, J. C. 2017, PASA, 34, e056
D'Orazi, V., Angelou, G. C., Gratton, R. G., et al. 2014, ApJ, 791, 39
D'Orazi, V., Gratton, R. G., Angelou, G. C., et al. 2015, MNRAS, 449, 4038
Fenner, Y., Gibson, B. K., Lee, H. C., et al. 2003, PASA, 20, 340
Fishlock, C. K., Karakas, A. I., Lugaro, M., & Yong, D. 2014, ApJ, 797, 44
Frebel, A., & Norris, J. E. 2015, ARA&A, 53, 631
Freytag, B., Ludwig, H.-G., & Steffen, M. 1996, A&A, 313, 497
Frost, C. A., & Lattanzio, J. C. 1996, ApJ, 473, 383
Fujimoto, M. Y., Iben, I., Jr, Chieffi, A., & Tornambe, A. 1984, ApJ, 287, 749
Fujimoto, M. Y., Ikeda, Y., & Iben, I., Jr 2000, ApJ, 529, L25
Garcia-Berro, E., & Iben, I. 1994, ApJ, 434, 306
Gavilán, M., Buell, J. F., & Mollá, M. 2005, A&A, 432, 861
Gavilán, M., Mollá, M., & Buell, J. F. 2006, A&A, 450, 509
Gay, P. L., & Lambert, D. L. 2000, ApJ, 533, 260
Gibson, B. K., Fenner, Y., Renda, A., Kawata, D., & Lee, H.-C. 2003, PASA, 20, 401
Gil-Pons, P., García-Berro, E., José, J., Hernanz, M., & Truran, J. W. 2003, A&A, 407, 1021
Gil-Pons, P., Suda, T., Fujimoto, M. Y., & García-Berro, E. 2005, A&A, 433, 1037

Gil-Pons, P., Gutierrez, J., & Garcia-Berro, E. 2008, in First Stars III, eds. B. W. O'Shea, & A. Heger, AIP Conf. Ser., 990, 241
Gil-Pons, P., Doherty, C. L., Lau, H., et al. 2013, A&A, 557, A106
Gil-Pons, P., Doherty, C. L., Gutiérrez, J. L., et al. 2018, PASA, 35, 38
Girardi, L., Bressan, A., Chiosi, C., Bertelli, G., & Nasi, E. 1996, A&AS, 117, 113
Goriely, S., & Siess, L. 2004, A&A, 421, L25
Grevesse, N., & Noels, A. 1993, in Origin and Evolution of the Elements, Symposium in Honour of Hubert Reeves' 60th birthday: Origin and evolution of the elements, eds. N. Prantzos, E. Vangioni-Flam, & M. Casse (Cambridge University Press), 15
Hale, S. E., Champagne, A. E., Iliadis, C., et al. 2002, Phys. Rev. C, 65, 015801
Hale, S. E., Champagne, A. E., Iliadis, C., et al. 2004, Phys. Rev. C, 70, 045802
Hansen, T., Hansen, C. J., Christlieb, N., et al. 2015, ApJ, 807, 173
Henkel, K., Karakas, A. I., & Lattanzio, J. C. 2017, MNRAS, 469, 4600
Herwig, F. 2004, ApJ, 605, 425
Herwig, F. 2005, ARA&A, 43, 435
Herwig, F., Langer, N., & Lugaro, M. 2003, ApJ, 593, 1056
Herwig, F., Woodward, P. R., Lin, P.-H., Knox, M., & Fryer, C. 2014, ApJ, 792, L3
Hirschi, R. 2007, A&A, 461, 571
Hirschi, R., Fröhlich, C., Liebendörfer, M., & Thielemann, F. -K., 2006, Rev. Mod. Astron., 19, 101
Iglesias, C. A., & Rogers, F. J. 1996, ApJ, 464, 943
Iliadis, C., D'Auria, J. M., Starrfield, S., Thompson, W. J., & Wiescher, M. 2001, ApJS, 134, 151
Iwamoto, N. 2009, PASA, 26, 145
Izzard, R., Lugaro, M., Illadis, C., & Karakas, A. 2006, International Symposium on Nuclear Astrophysics – Nuclei in the Cosmos, 38.1
Jones, S., Hirschi, R., Nomoto, K., et al. 2013, ApJ, 772, 150
Jorissen, A., & Arnould, M. 1989, A&A, 221, 161
Karakas, A. I. 2010, MNRAS, 403, 1413
Karakas, A. I., & Lattanzio, J. C. 2003, PASA, 20, 279
Karakas, A., & Lattanzio, J. C. 2007, PASA, 24, 103
Karakas, A. I., & Lattanzio, J. C. 2014, PASA, 31, e030
Karakas, A. I., Lugaro, M. A., Wiescher, M., Görres, J., & Ugalde, C. 2006, ApJ, 643, 471
Keller, S. C., Schmidt, B. P., Bessell, M. S., et al. 2007, PASA, 24, 1
Kippenhahn, R., Ruschenplatt, G., & Thomas, H. C. 1980, A&A, 91, 175
Kobayashi, C., Umeda, H., Nomoto, K., Tominaga, N., & Ohkubo, T. 2006, ApJ, 653, 1145
Kobayashi, C., Karakas, A. I., & Umeda, H. 2011, MNRAS, 414, 3231
Kobayashi, C., Karakas, A. I., & Lugaro, M. 2020, ApJ, 900, 179
Kroupa, P. 2001, MNRAS, 322, 231
Lagadec, E., & Zijlstra, A. A. 2008, MNRAS, 390, L59
Lau, H. H. B., Stancliffe, R. J., & Tout, C. A. 2008, MNRAS, 385, 301
Lau, H. H. B., Stancliffe, R. J., & Tout, C. A. 2009, MNRAS, 396, 1046
Lau, H. H. B., Gil-Pons, P., Doherty, C., & Lattanzio, J. 2012, A&A, 542, A1
Lederer, M. T., & Aringer, B. 2009, A&A, 494, 403
Lugaro, M., Herwig, F., Lattanzio, J. C., Gallino, R., & Straniero, O. 2003, ApJ, 586, 1305
Lugaro, M., Ugalde, C., Karakas, A. I., et al. 2004, ApJ, 615, 934
Marigo, P. 2001, A&A, 370, 194
Marigo, P. 2002, A&A, 387, 507
Marigo, P., & Girardi, L. 2007, A&A, 469, 239
Marigo, P., & Aringer, B. 2009, A&A, 508, 1539
Marigo, P., Girardi, L., Chiosi, C., & Wood, P. R. 2001, A&A, 371, 152
Matteucci, F., Spitoni, E., Romano, D., & Rojas Arriagada, A. 2016, Frontier Research in Astrophysics II, held 23–28 May, 2016 in Mondello (Palermo), Italy (FRAPWS2016), 27, id. 27, https://pos.sissa.it/cgi-bin/reader/conf.cgi?confid=269
Mattsson, L., Wahlin, R., Höfner, S., & Eriksson, K. 2008, A&A, 484, L5
Meléndez, J., & Cohen, J. G. 2007, ApJ, 659, L25
Meléndez, J., & Cohen, J. G. 2009, ApJ, 699, 2017
Meynet, G., & Maeder, A. 2002, A&A, 390, 561
Meynet, G., Ekström, S., & Maeder, A. 2006, A&A, 447, 623
Millán-Irigoyen, I., Mollá, M., & Ascasibar, Y. 2020, MNRAS, 494, 146
Miller, G. E., & Scalo, J. M. 1979, ApJS, 41, 513
Milone, A. P., Marino, A. F., Cassisi, S., et al. 2012, ApJ, 754, L34

Milone, A. P., Marino, A. F., Dotter, A., et al. 2014, ApJ, 785, 21
Mocák, M., Campbell, S. W., Müller, E., & Kifonidis, K. 2010, A&A, 520, A114
Mollá, M., Cavichia, O., Gavilán, M., & Gibson, B. K. 2015, MNRAS, 451, 3693
Nanni, A. 2018, MNRAS, 482, 4726
Norris, J. E. 2004, ApJ, 612, L25
Nucci, M. C., & Busso, M. 2014, ApJ, 787, 141
Pauldrach, A. W. A., Kudritzi, R. P., & Puls, J. 1989, in Astronomische Gesellschaft Abstract Series, Astron. Gesell. Abstr. Ser., 3, 47
Piotto, G., Bedin, L. R., Anderson, J., et al. 2007, ApJ, 661, L53
Piotto, G., Milone, A. P., Anderson, J., et al. 2012, ApJ, 760, 39
Piotto, G., Milone, A. P., Marino, A. F., et al. 2013, ApJ, 775, 15
Prantzos, N., Abia, C., Limongi, M., Chieffi, A., & Cristallo, S. 2018, MNRAS, 476, 3432
Reimers, D. 1975, Mem. Soc. R. Sci. Liege, 8, 369
Ritter, C., Herwig, F., Jones, S., et al. 2018, MNRAS, 480, 538
Romano, D., Matteucci, F., Zhang, Z. Y., Papadopoulos, P. P., & Ivison, R. J. 2017, MNRAS, 470, 401
Salpeter, E. E. 1955, ApJ, 121, 161
Siess, L. 2006, A&A, 448, 717
Siess, L. 2010, A&A, 512, A10
Siess, L., Livio, M., & Lattanzio, J. 2002, ApJ, 570, 329
Simon, J. D. 2019, ARA&A, 57, 375
Sivarani, T., Beers, T. C., Bonifacio, P., et al. 2006, A&A, 459, 125
Spite, M., Cayrel, R., Hill, V., et al. 2006, A&A, 455, 291
Spite, M., Caffau, E., Bonifacio, P., et al. 2013, A&A, 552, A107
Spitoni, E., Vincenzo, F., & Matteucci, F. 2017, A&A, 599, A6
Stancliffe, R. J., Glebbeek, E., Izzard, R. G., & Pols, O. R. 2007, A&A, 464, L57
Stancliffe, R. J., Chieffi, A., Lattanzio, J. C., & Church, R. P. 2009, PASA, 26, 203
Starkenburg, E., Martin, N., Youakim, K., et al. 2017, MNRAS, 471, 2587
Straniero, O., Chieffi, A., Limongi, M., et al. 1997, ApJ, 478, 332
Straniero, O., Domínguez, I., Cristallo, S., & Gallino, R. 2003, PASA, 20, 389
Straniero, O., Gallino, R., & Cristallo, S. 2006, Nucl. Phys. A, 777, 311
Straniero, O., Cristallo, S., & Piersanti, L. 2014, ApJ, 785, 77
Straniero, O., Cristallo, S., & Piersanti, L. 2015, in Why Galaxies Care about AGB Stars III: A Closer Look in Space and Time, eds. F. Kerschbaum, R. F. Wing, & J. Hron, ASP Conf. Ser., 497, 259
Suda, T., & Fujimoto, M. Y. 2010, MNRAS, 405, 177
Suda, T., Aikawa, M., Machida, M. N., Fujimoto, M. Y., & Iben, I., Jr 2004, ApJ, 611, 476
Suda, T., Katsuta, Y., Yamada, S., et al. 2008, PASJ, 60, 1159
Suda, T., Yamada, S., Katsuta, Y., et al. 2011, MNRAS, 412, 843
Suda, T., Komiya, Y., Yamada, S., et al. 2013, MNRAS, 432, 46
Suda, T., Hidaka, J., Aoki, W., et al. 2017, PASJ, 69, 76
Thielemann, F. K., Arnould, M., & Truran, J. W. 1986, Max Planck Institut fur Astrophysik Report, 262
Timmes, F. X., Woosley, S. E., & Weaver, T. A. 1995, ApJS, 98, 617
Tsujimoto, T., & Bekki, K. 2012, ApJ, 747, 125
Umeda, H., & Nomoto, K. 2005, ApJ, 619, 427
van den Hoek, L. B., & Groenewegen, M. A. T. 1997, A&AS, 123
Vangioni, E., & Olive, K. A. 2019, MNRAS, 484, 3561
Vassiliadis, E., & Wood, P. R. 1993, ApJ, 413, 641
Ventura, P., & D'Antona, F. 2005, A&A, 431, 279
Ventura, P., & D'Antona, F. 2010, MNRAS, 402, L72
Ventura, P., D'Antona, F., & Mazzitelli, I. 2000, A&A, 363, 605
Ventura, P., D'Antona, F., Mazzitelli, I., & Gratton, R. 2001, ApJ, 550, L65
Ventura, P., García-Hernández, D. A., Dell'Agli, F., et al. 2016, ApJ, 831, L17
Ventura, P., D'Antona, F., Imbriani, G., et al. 2018, MNRAS, 477, 438
Vincenzo, F., Belfiore, F., Maiolino, R., Matteucci, F., & Ventura, P. 2016, MNRAS, 458, 3466
Woodward, P. R., Herwig, F., & Lin, P.-H. 2015, ApJ, 798, 49
Yamada, S., Suda, T., Komiya, Y., Aoki, W., & Fujimoto, M. Y. 2013, MNRAS, 436, 1362
Yanny, B., Rockosi, C., Newberg, H. J., et al. 2009, AJ, 137, 4377
Yong, D., Lambert, D. L., & Ivans, I. I. 2003, ApJ, 599, 1357
Zackrisson, E., Rydberg, C.-E., Schaerer, D., Östlin, G., & Tuli, M. 2011, ApJ, 740, 13

Appendix A: Model abundances in terms of ejecta

The abundance patterns of selected elements in terms of [X/Fe], which may facilitate comparison with observational data and with other theoretical calculations, are presented in Table A.1.

We note that the results corresponding to our actual yields are presented in Fig. 7, and those corresponding to the hypothetical cases in which 1% of the matter ejected by our models is homogeneously mixed in the $0.2\,M_\odot$ envelope of an unevolved $Z = 10^{-5}$ star, are presented in Figs. 11 and 12.

Table A.1. Abundances pattern of selected elements in terms of [X/Fe] as given by the ejecta, or under the assumption that 1% of this matter was homogeneously diluted in the surface $0.2\,M_\odot$ of an unevolved $Z = 10^{-5}$ star.

$M_{\rm ini}/M_\odot$	$\langle\log_{10}(^7{\rm Li})\rangle$	C	N	O	F	Ne	Na	Mg	Al	Si	P	S
						VW93						
3.0	−0.49	3.19	4.97	2.30	3.74	3.85	3.95	3.73	3.35	2.15	2.62	0.29
3.0-dil	−0.04	2.14	3.91	1.27	2.69	2.80	2.90	2.68	2.30	1.13	1.57	0.02
4.0	−0.13	3.14	4.91	2.36	2.95	3.48	3.66	3.77	3.56	2.28	3.06	0.65
4.0-dil	−0.03	2.07	3.84	1.31	1.89	2.42	2.59	2.71	2.49	1.24	2.00	0.11
5.0	−0.44	2.98	4.85	2.20	2.66	3.31	3.41	3.61	3.70	2.24	3.03	0.63
5.0-dil	−0.05	2.18	4.04	1.41	1.86	2.51	2.61	2.81	2.90	1.45	2.23	0.18
6.0	−0.46	2.78	4.75	2.04	1.93	2.96	2.92	3.39	3.64	2.04	2.76	0.43
6.0-ms	−0.06	2.07	4.03	1.34	1.24	2.25	2.21	2.67	2.92	1.34	2.05	0.12
7.0	−0.49	2.69	4.54	1.87	1.46	2.49	2.36	3.07	3.35	1.95	2.55	0.34
7.0-dil	−0.07	2.04	3.88	1.23	0.85	1.84	1.71	2.42	2.69	1.31	1.90	0.10
						Blo95						
3.0	2.58	3.61	3.67	1.61	3.37	2.51	2.36	2.28	1.56	0.57	0.88	5.6×10^{-3}
3.0-dil	1.55	2.59	2.65	0.68	2.35	1.50	1.36	1.28	0.64	0.10	0.21	5.4×10^{-3}
4.0	1.50	2.72	4.18	1.54	2.46	2.26	2.26	2.20	1.68	0.55	1.03	9.2×10^{-3}
4.0-dil	0.68	1.85	3.30	0.74	1.59	1.40	1.39	1.34	0.86	0.13	0.36	9.2×10^{-3}
5.0	0.94	2.42	3.99	1.30	1.77	1.90	1.91	1.92	1.64	0.38	0.94	8.0×10^{-3}
5.0-dil	0.32	1.65	3.22	0.62	1.03	1.15	1.16	1.17	0.91	0.09	0.36	1.4×10^{-3}
6.0 ($\eta = 0.02$)	0.49	2.23	3.88	1.43	1.81	1.45	1.29	1.70	1.60	0.31	0.76	5.8×10^{-3}
6.0-dil ($\eta = 0.02$)	0.12	1.54	3.18	0.79	1.14	0.81	0.68	1.03	0.94	0.08	0.29	1.2×10^{-3}
6.0 ($\eta = 0.04$)	0.67	2.22	3.71	1.13	1.42	1.24	1.14	1.32	1.26	0.16	0.49	2.1×10^{-3}
6.0-dil ($\eta = 0.04$)	0.23	1.53	3.02	0.54	0.78	0.63	0.55	0.70	0.64	0.04	0.15	4.2×10^{-4}
6.0 ($\eta = 1$)	2.16	1.17	2.67	0.17	−0.37	0.02	0.41	0.10	0.29	0.03	0.20	4.1×10^{-5}
6.0-dil ($\eta = 1$)	1.47	0.58	1.98	0.04	−0.05	0.00	0.12	0.02	0.08	0.01	0.05	8.4×10^{-6}
7.0	−0.32	2.41	3.49	1.00	1.00	1.00	0.94	1.37	1.14	0.50	0.59	6.9×10^{-3}
7.0-dil	−0.07	1.77	2.85	0.49	0.49	0.49	0.44	0.79	0.59	0.17	0.22	1.6×10^{-3}
7.5	−0.55	1.08	3.79	−0.46	−0.80	−0.11	−0.97	−1.00	−0.90	0.49	−0.31	7.9×10^{-3}
7.5-dil	−0.09	0.56	3.17	−0.07	−0.10	−0.02	−0.11	−0.11	−0.10	0.18	−0.06	1.9×10^{-3}

Notes. Lithium abundance is shown as $\langle\log_{10}(^7{\rm Li})\rangle = {\rm Log}_{10}(N({\rm Li})/N({\rm H})) + 12$. Results using the Vassiliadis & Wood (1993) and Bloecker (1995) with the indicated η values are shown.